Realistic Electronic Structure Calculations for Quantum Materials

Realistic Electronic Structure Calculations for Quantum Materials

by

Addison Richards

A thesis submitted to the School of Graduate Studies
in partial fulfillment of the requirements for the degree of
Master of Science in Physics and Astronomy

McMaster University © Addison Richards 2023

McMaster University
Master of Science (2023)
Hamilton, Ontario (Department of Physics and Astronomy)

TITLE: Realistic Electronic Structure Calculations for Quantum Materials
AUTHOR: Addison Richards (McMaster University)
SUPERVISOR: Dr. Erik Sørensen
NUMBER OF PAGES: x, 50

Abstract

A complex arrangement of electronic states within materials can manifest exotic quantum-mechanical effects. These systems are often referred to as quantum materials. Increased understanding of quantum materials has historically lead to the development of new technologies. It is therefore extremely important to develop and test precise methods for calculating the behaviour of electronic states within a material.

For decades, the workhorse of electronic structure calculations has been density functional theory (DFT). DFT is often referred to as a first-principles method because it allows for the calculation of the distribution of electrons throughout a material with only specification of the lattice geometry and atomic components. From the results of a DFT calculation, it is possible to study the orbital character of electronic wavefunctions, topology of electronic band structure, and some aspects of superconductivity. This provides insight into many quantum properties of a system which may otherwise be difficult or impossible to ascertain from experiments. DFT is, however, sometimes limited by the approximations necessary for practical implementation. Further methods have been developed to systematically correct the limitations of DFT. In particular, the combination of DFT with dynamical mean-field theory (DFT+DMFT) is among the most widely accepted methods for correcting the inadequacy of DFT in handling strong electron-electron correlations. In this thesis, I use methods from DFT and DFT+DMFT to study the quantum properties of materials.

Acknowledgements

First and foremost, I would like to thank my supervisor, Erik Sørensen, who has provided me with the opportunity to study the subject that I love and has supported me throughout the coronavirus pandemic. I am grateful for the guidance that Erik has provided to me on a regular basis, coupled with the freedom to explore many of my own research interests independently. The other graduate students within the group, James, Jon, Yannick, and Sebastien, have acted as both friends and a consistent source of inspiration. I have also benefited from discussions and collaborations with the experimentalists at McMaster. In particular, Sudarshan Sharma and Graeme Luke have each introduced me to interesting materials which are the main subjects of this thesis, and I have benefited from discussions with them about experimental observations for these materials. I appreciate that this has allowed me to keep my research grounded in reality. I would like to thank my committee members, Paul Ayers and Graeme Luke, for taking the time to read this thesis and for providing me with insightful discussions. My experience as a graduate student has also been enriched by the many amazing friends that I have had the privilege of meeting within McMaster, across Canada, and internationally. I attribute a significant amount of my passion and understanding of physics to discussions with these people. I will not enumerate them all out of fear of missing someone, but I will say that my time at McMaster so far would certainly not have been as enjoyable without Symphony Huang and Sudarshan Sharma here. Finally, I would like to thank the physics department as a whole for providing a friendly and very supportive environment to work in.

Table of Contents

List of Figures

List of Tables

Chapter 0

Preface

In this work, quantum materials are studied within the context of electronic structure theory. I have studied three separate cases in particular. I will present original results and conclusions for each case in chapters 2-4 based on electronic structure calculations which I have performed. Throughout this work, I have benefited greatly from discussions and collaborations with Sudarshan Sharma and Graeme Luke. They have introduced me to materials which are the primary subjects of chapters 2-4.

In Chapter 1, I present standard methods for calculating the electronic structure of quantum materials as well as methods for analyzing the results. In Chapter 2, I discuss the nature of the superconducting state for two related materials, TaRuSi and TaReSi. TaRuSi has been shown to break time-reversal symmetry in the superconducting state [43, 42] while TaReSi does not [43]. I argue based on symmetry analysis and density functional theory calculations that the superconducting state likely originates from a non-unitary triplet-pairing mechanism. In Chapter 3, I analyse the band structure topology of the series of disordered materials, $BiPd_{1-x}Pt_x$, and present the results of a surface-state spectral function calculation revealing surface-state Dirac cones. In Chapter 4, I present the correlated electronic spectral function for the metallic Kagome-lattice material, YCr_6Ge_6, obtained from the combination of density functional theory and dynamical mean-field theory calculations. The result shows evidence that a coherent flat band state with very low electronic dispersion exists near the Fermi energy in this material. Finally, I end with some concluding remarks in Chapter 5.

Chapter 1

Electronic Structure Theory

1.1 Overview

1.1.1 Band Theory and the Tight-Binding Model

Shortly after the formulation of quantum mechanics, Bloch's theorem demonstrated that non-interacting electrons in an arbitrary periodic potential can be characterized by good quantum numbers $\mathbf{k}$ and ν, often referred to as wavevector or crystal momentum and band index respectively. An electron wavevector is uniquely defined by a point within the first Brillouin zone of the system, and the band index labels the energy levels corresponding with each wavevector. This characterization of electron states in a periodic potential is known as band theory. The Pauli exclusion principle then dictates that the ground state of an N-electron system is obtained by filling the N lowest energy states.

Two important and somewhat opposite models were then introduced to describe the electronic structure of materials. The first is the homogenous electron gas in which electrons contributing to conduction are viewed as separate from ions which form the periodic lattice structure of the material. The second is the tight binding model in which solids are described as a combination of localized atomic or molecular orbitals. The homogeneous electron gas model provides a reasonable description of alkali metals, for example, since there is only one electron in the valence shell of an alkali-metal atom which is weakly bound to the nucleus. In the tight-binding model, conduction is a consequence of the increased electron tunneling amplitude between atomic orbitals as the orbitals are brought into close proximity. Of course, these models constitute two extreme limits, and are too oversimplified to describe many of the properties of real materials. In Section 1.2, I will show how modern electronic structure theory is capable of taking both

of these concepts into account. In particular, the homogeneous electron gas picture is the starting point in the development of the local-density approximation of density-functional theory and the tight-binding model is the starting point for the Hubbard model and dynamical mean-field theory.

The simplest one-band tight-binding model Hamiltonian describing non-interacting electrons which allows electron tunnelling between orbitals is

$$H = \sum_{ij\sigma} t_{ij} c^{\dagger}_{i\sigma} c_{j\sigma} = \frac{V}{(2\pi)^3} \int_{BZ} \epsilon(\mathbf{k}) n_{\mathbf{k}\sigma} \tag{1.1}$$

where t_{ij} is the tunneling amplitude for electrons hopping from orbitals centered on lattice site j to site i, $c_{i\sigma}$ is the electron annihilation operator for orbital at lattice site, i, and spin, σ, $\epsilon(\mathbf{k}) = \sum_{\mathbf{r}_{ij}} t_{ij} e^{-i\mathbf{k}\cdot\mathbf{r}_{ij}}$ is referred to as the dispersion energy or band structure, $\mathbf{r}_{ij}$ is the distance between orbitals centered at site i and j, V is the volume of the system, and $n_{\mathbf{k}\sigma}$ is the number operator for electrons occupying a Bloch state labelled by $\mathbf{k}$. From this we can see that $[H, n_{\mathbf{k}\sigma}] = 0$ and therefore the Bloch state occupation number, $n_{\mathbf{k}\sigma}$, is conserved.

1.1.2 The Hubbard Model

The Hubbard model is a simple modification of the tight-binding model and is defined by the Hamiltonian

$$H = \sum_{ij\sigma} t_{ij} c^{\dagger}_{i\sigma} c_{j\sigma} + U \sum_{i} n_{i\uparrow} n_{i\downarrow} \tag{1.2}$$

where $n_{i\sigma} = c^{\dagger}_{i\sigma} c_{i\sigma}$ is the number operator for electrons occupying an orbital located at site i with spin σ. The Hubbard model therefore can be thought of as the tight-binding model with an additional energy increase for any doubly-occupied orbitals. The double-occupation energy, U, is the electron-electron Coulomb repulsion experienced by electrons occupying the same orbital. In this case, $[H, n_{\mathbf{k}\sigma}] \neq 0$, and the ground-state wavefunction does not have a natural description in terms of Bloch states. While the tight-binding model is easy to solve, the Hubbard model, despite its simplicity, is one of the most difficult models to solve in dimensions greater than one. The ability to accurately calculate the ground-state or excitation spectra for the Hubbard model is a relatively recent development, requiring advanced modern numerical methods, often giving only an approximate solution.

The Hubbard model description of a material addresses and corrects major qualitative flaws of band theory. The most obvious failure of band theory, in many cases, is its characterization of insulators. Since band theory states that

Bloch electrons occupy the lowest energy states permitted by the Pauli exclusion principle, any system with an odd number of electrons per unit cell is bound to have a partially-filled band and is therefore a conductor. This is not the case in reality, and one can find many examples of insulating systems with an odd number of electrons per unit cell. A remedy to this problem arises naturally in the Hubbard model. As U is increased, electrons will tend to remain localized on an orbital when hopping between orbitals would result in double occupation. Once a critical value of U is reached, the system becomes an insulator. This insulating state is referred to as a Mott insulator. Significant electron-electron Coulomb repulsion can also have drastic effects on a metallic state. For example, satellite peaks can sometimes be observed in electronic excitation spectra measurement, often referred to as Hubbard bands, and the observed renormalization of band structure when compared with band structure obtained from band theory calculations.

1.2 Methods of Electronic Structure Theory

The many-body Schrodinger equation describing any arrangement of atoms at positions, $\mathbf{R}$, with atomic numbers, $Z_{\mathbf{R}}$, is

$$\sum_{\mathbf{R},\mathbf{r}} \left[-\frac{\hbar^2}{2m_{\mathbf{R}}}\nabla^2_{\mathbf{R}} - \frac{\hbar^2}{2m_e}\nabla^2_{\mathbf{r}} + \frac{Z_{\mathbf{R}}e^2}{|\mathbf{R}-\mathbf{r}|} + \sum_{\mathbf{R}'\neq\mathbf{R}} \frac{Z_{\mathbf{R}}Z_{\mathbf{R}'}e^2}{|\mathbf{R}-\mathbf{R}'|} + \sum_{\mathbf{r}'\neq\mathbf{r}} \frac{e^2}{|\mathbf{r}-\mathbf{r}'|} \right] \Psi = E\Psi \tag{1.3}$$

In theory, the solution of this equation should describe all properties of matter which are not significantly affected by relativistic effects. However, this equation is impossible to solve for a system resembling a real material. We can simplify this equation slightly by noticing that the mass of an atomic nucleus is several orders of magnitude greater than the electron mass. That is, we can apply the Born-Oppenheimer approximation in which the kinetic energy of atomic nuclei is ignored completely, effectively taking $m_{\mathbf{R}} \to \infty$. If we treat the atomic nuclei as static in this way, then the equation defining the many-body electronic wavefunction is

$$\sum_{\mathbf{r}} \left[-\frac{\hbar^2}{2m_e}\nabla^2_{\mathbf{r}} + V^{\mathrm{Ion}}(\mathbf{r}) + \sum_{\mathbf{r}'\neq\mathbf{r}} V^{\mathrm{ee}}(\mathbf{r},\mathbf{r}') \right] \Psi_{\mathrm{e}} = E_{\mathrm{e}}\Psi_{\mathrm{e}} \tag{1.4}$$

where $V^{\mathrm{Ion}}(\mathbf{r}) = \sum_{\mathbf{R}} \frac{Z_{\mathbf{R}}e^2}{|\mathbf{R}-\mathbf{r}|}$ is the Coulomb interaction between atomic nuclei and electrons, and $V^{\mathrm{ee}}(\mathbf{r},\mathbf{r}') = \frac{e^2}{|\mathbf{r}-\mathbf{r}'|}$ is the electron-electron Coulomb repulsion.

In following sections, I will briefly explain the implementation of some methods for calculating and analyzing electronic structure. In the following chapters, I will apply the methods presented in the section, where applicable, to calculate the electronic structure for quantum materials of current research interest.

1.2.1 Density Functional Theory

The Hohenberg-Kohn (HK) theorems suggested that direct calculation of electronic structure may be feasible. The HK theorems are as follows:

Hohenberg-Kohn Theorems:

1. The external potential, $V^{\text{ext}}(\mathbf{r})$, and therefore the total energy, is a unique functional of the charge density, $n(\mathbf{r})$.
2. The charge density which minimizes the total energy functional is the exact ground-state charge density.

The HK theorems imply that, for a given system, we can define an energy functional, $E[n]$, such that, when $n(\mathbf{r})$ minimizes $E[n]$, then $n(\mathbf{r})$ is the ground-state charge density. This result enabled the development of practical methods for calculating electronic properties of materials based on the charge density. In particular, density functional theory (DFT) applied to systems of electrons as formulated by Kohn and Sham for calculating ground-state charge densities, which I will simply refer to as DFT, is justified by the HK theorems.

The implementation of DFT is as follows: First define an auxiliary set of orbitals, $\{\psi_i(\mathbf{r})\}$, often referred to as Kohn-Sham (KS) orbitals. The KS orbitals are not meant to represent single-electron wavefunctions, but will be used for determining the charge density. The equations, called the KS equations, enforcing total-energy minimization subject to the orthonormalization of the KS orbitals constraint, are given by

$$\left[-\frac{\hbar^2}{2m_e}\nabla^2 + V^{\text{ext}}[n](\mathbf{r})\right]\psi_i(\mathbf{r}) = \epsilon_i\psi_i(\mathbf{r}). \tag{1.5}$$

After a set of ϵ_i and ψ_i are obtained through solution of the KS equations, we can obtain the charge density as $n(\mathbf{r}) = \sum_i |\psi_i(\mathbf{r})|^2$, and an updated estimate for the external potential, $V^{\text{ext}}[n]$, can be computed. This procedure can then be repeated until further iterations produce no change in the external potential. The charge density, $n(\mathbf{r})$, is then consistent with the total energy minimization presumption. For periodic systems, Bloch's theorem is used to allow a practical implementation of the DFT cycle, so that the index, i, labels a band, wavevector, and spin, $i = (\nu, \mathbf{k}, \sigma)$. After the charge density has been determined, the Hellman-Feynman theorem can be used to calculated forces acting on each atom. This allows for the structural relaxation of atomic positions by the gradient descent method and perturbative calculation of phonon spectra.

While the above scheme provides a method for computing the ground-state charge density, the exact form of the external potential, $V^{\text{ext}}[n]$, to be used is still unclear. In general, the external potential must be approximated, typically

through relations to exact solutions of simpler systems. The general form of the external potential can be written as

$$V^{\text{ext}}[n](\mathbf{r}) = V^{\text{Ion}}(\mathbf{r}) + V^{\text{H}}[n](\mathbf{r}) + V^{\text{xc}}[n](\mathbf{r}) \tag{1.6}$$

where V^{Ion} is the same ionic potential defined previously, V^{H} is the Hartree potential,

$$V^{\text{H}}[n](\mathbf{r}) = e^2 \int d^3r' \frac{n(\mathbf{r}')}{|\mathbf{r} - \mathbf{r}'|} \tag{1.7}$$

and V^{xc} is referred to as the exchange-correlation potential. V^{xc} encompasses all contributions to the external potential which are not captured by the ionic or Hartree potentials. In the Hartree-Fock approximation, correlation is neglected, and the exchange potential may be written as an integral operator

$$V_x \psi_i(\mathbf{r}) = e^2 \sum_j \int d^3r' \frac{\psi_j^*(\mathbf{r}')\psi_j(\mathbf{r})}{|\mathbf{r} - \mathbf{r}'|} \psi_i(\mathbf{r}') \tag{1.8}$$

While the exchange energy may be computed exactly in this way, this term is incompatible with the KS equations and is computationally expensive. Additionally, the neglect of correlations often gives poor agreement with experimentally-determined quantities, such as equilibrium lattice constants.

A feasible method for including both of the exchange and correlation potentials, called the local density approximation (LDA), was proposed by Kohn and Sham [22] and is still widely used. The idea is implemented by relating the exchange-correlation potential to that of a parameterized solution of the exchange-correlation potential for a homogeneous electron gas with parameters determined exactly from quantum Monte Carlo [7]. This method is semi-local in the sense that the exchange-correlation energy can be expressed as

$$E^{\text{xc}}[n] = \int d^3r \; \epsilon^{\text{xc}}(n(\mathbf{r}))n(\mathbf{r}) \tag{1.9}$$

where ϵ^{xc} is a local exchange-correlation energy which only depends on the charge density.

Today, there exists over a hundred different approximations to the external potential, the most prevalent of which are the LDA, and an extension of the LDA including corrections due to density gradients called the generalized gradient approximation (GGA). Meta-GGA methods improve upon GGA by including further corrections due to kinetic energy density. Hybrid extensions of DFT additionally include a fraction of the exact exchange energy. The LDA and GGA often provide

an accurate description of weakly-correlated materials, but fail at capturing even qualitative features of strongly-correlated materials.

Relativistic corrections are typically included in DFT calculations. This is achieved by considering the many-body Dirac equation in place of the Schrodinger equation. When spin-orbit coupling is neglected, incorporating relativistic corrections amounts to a simple modification of the non-relativistic energy functional as shown in Ref.[21]. A DFT calculation based on this scheme is usually referred to as scalar relativistic or "without spin-orbit coupling". The inclusion of spin-orbit coupling in the DFT energy functional requires the Kohn-Sham orbitals to be treated as a Dirac spinors. For example, as is described in Ref.[27]. A DFT calculation based on this scheme is usually referred to as fully relativistic or "with spin-orbit coupling". DFT calculations presented in this thesis are without spin-orbit coupling unless otherwise stated.

1.2.2 Wannier Functions

Self-consistent solution of the KS equations produces a set of Bloch orbitals, $\psi^{\sigma}_{\nu\mathbf{k}}$, often referred to as KS orbitals, where ν, $\mathbf{k}$, and σ, are the band index, crystal momentum, and spin quantum numbers respectively. Although these are not exact wavefunctions of single electrons, they provide a useful basis for realistic model Hamiltonian construction. Given that the phase of each KS orbital does not affect the ground-state charge density, a new basis set can be constructed through a unitary transformation,

$$|\phi^{\sigma}_{n\mathbf{k}}\rangle = \sum_{\nu} U_{n\nu}(\mathbf{k})|\psi^{\sigma}_{\nu\mathbf{k}}\rangle, \tag{1.10}$$

where $U_{n\nu}$ is an arbitrary unitary matrix. Wannier functions centered at position $\mathbf{R}$ are then defined as

$$|\phi^{\sigma}_{n\mathbf{R}}\rangle = \frac{V}{(2\pi)^3}\int d^3k e^{-i\mathbf{k}\cdot\mathbf{R}}|\phi^{\sigma}_{n\mathbf{k}}\rangle. \tag{1.11}$$

A unique set of Wannier functions called maximally-localized Wannier functions can be obtained by minimizing the spread functional,

$$\Omega[\{\phi^{\sigma}_{n\mathbf{0}}\}] = \sum_{n\sigma}\langle\phi^{\sigma}_{n\mathbf{0}}|r^2|\phi^{\sigma}_{n\mathbf{0}}\rangle - \langle\phi^{\sigma}_{n\mathbf{0}}|r|\phi^{\sigma}_{n\mathbf{0}}\rangle^2. \tag{1.12}$$

Additionally, a disentanglement spread functional needs to be minimized when the number of Wannier functions per unit cell is less than the number of bands included in the Wannier function calculation. Extensive implementation details are given in Ref. [29].

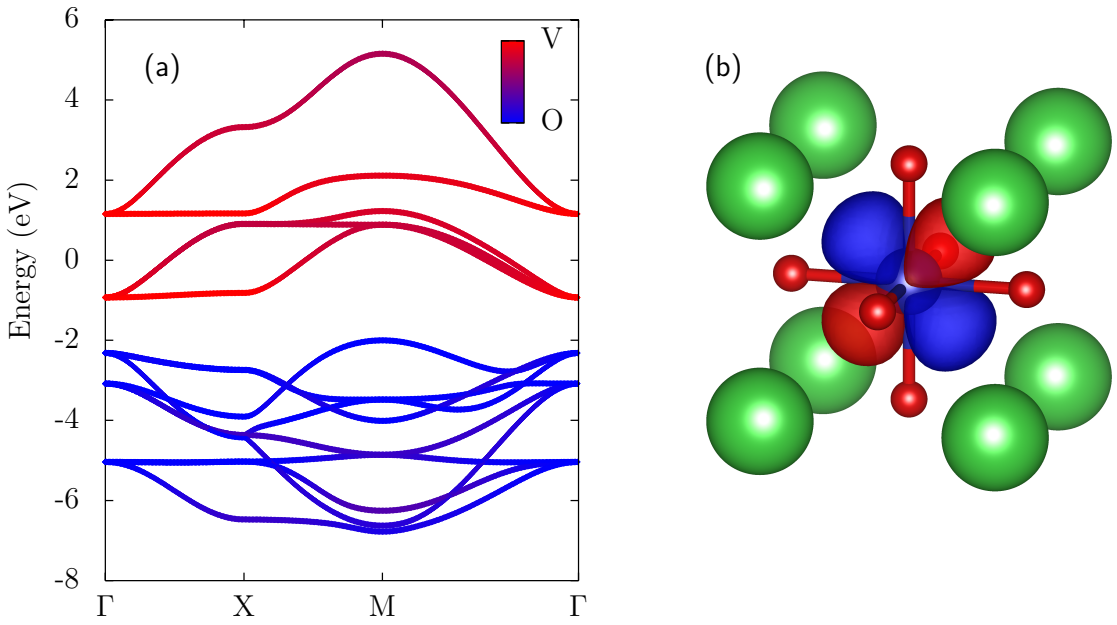

Figure 1.1: (a) DFT band structure for $SrVO_3$ and (b) Maximally-localized Wannier function for one of the V-t_{2g} orbitals within the unit cell of $SrVO_3$. Sr, V, and O atoms are represented by green, blue, and red sites respectively. Colouring of the band structure is obtained by projection onto Wannier-orbitals centered on V (red) and O (blue) sites.

As an example, the DFT band structure from $SrVO_3$ is plotted in Fig. 1.1, with bands coloured according to the projection onto Wannier orbitals. The DFT bands are obtained using the Quantum Espresso software library [13] and Wannier functions are obtained using Wannier90 [31]. One of the t_{2g} Wannier function formed primarily from the three bands closest to the Fermi energy is also plotted. It can be seen that the maximally-localized Wannier function is qualitatively very similar to an atomic orbital centered on the V atom. Wannier orbitals therefore provide a useful basis for constructing material-specific Hubbard-like models.

1.2.3 Electronic Correlations and DFT+U

Given a complete set of orbitals, $\{\phi_{\mathbf{R}i}(\mathbf{r})\}$, the most general electronic Hamiltonian can be written in second-quantized notation as

$$H_e = -\sum_{\mathbf{R}\mathbf{R}'}\sum_{ij} t_{ij}^{\mathbf{R}\mathbf{R}'} c_{\mathbf{R}i}^\dagger c_{\mathbf{R}'j} + \frac{1}{2}\sum_{\mathbf{R}\mathbf{R}'\mathbf{R}''\mathbf{R}'''}\sum_{ijkl} U_{ijkl}^{\mathbf{R}\mathbf{R}'\mathbf{R}''\mathbf{R}'''} c_{\mathbf{R}i}^\dagger c_{\mathbf{R}'j}^\dagger c_{\mathbf{R}''k} c_{\mathbf{R}'''l} \tag{1.13}$$

where $\mathbf{R}, \mathbf{R}', \mathbf{R}''$, and $\mathbf{R}'''$ label atomic positions, i, j, k, and l label sets of spin/orbital indices, $c_{\mathbf{R}i}$ are annihilation operators for an electron occupying orbital $\phi_{\mathbf{R}i}$,

$$t_{ij}^{\mathbf{R}\mathbf{R}'} = -\int d^3r \phi_{\mathbf{R}i}^*(\mathbf{r}) \left(-\frac{\hbar^2}{2m_e}\nabla^2 - \sum_{\mathbf{R}} \frac{Z_{\mathbf{R}} e^2}{|\mathbf{r}-\mathbf{R}|}\right) \phi_{\mathbf{R}'j}(\mathbf{r}) \tag{1.14}$$

and

$$U_{ijkl}^{\mathbf{R}\mathbf{R}'\mathbf{R}''\mathbf{R}'''} = \int d^3r_1 \int d^3r_2 \phi_{\mathbf{R}i}^*(\mathbf{r}_1)\phi_{\mathbf{R}'j}^*(\mathbf{r}_2)\frac{e^2}{|\mathbf{r}_1-\mathbf{r}_2|}\phi_{\mathbf{R}''k}(\mathbf{r}_2)\phi_{\mathbf{R}'''l}(\mathbf{r}_1) \tag{1.15}$$

Upon making the substitution, $t_{ij}^{\mathbf{R}\mathbf{R}'} \to \tilde{t}_{ij}^{\mathbf{R}\mathbf{R}'}$, with

$$\tilde{t}_{ij}^{\mathbf{R}\mathbf{R}'} = -\int d^3r \phi_{\mathbf{R}i}^*(\mathbf{r}) \left(-\frac{\hbar^2}{2m_e}\nabla^2 + V^{\text{ext}}[n](\mathbf{r})\right) \phi_{\mathbf{R}'j}(\mathbf{r}), \tag{1.16}$$

it is easy to see that the $t_{ij}^{\mathbf{R}\mathbf{R}'}$ define a tight-binding model for the DFT Hamiltonian in the basis of the $\phi_{\mathbf{R}i}$ orbitals. The electronic Hamiltonian can then be written equivalently as

$$H_e = -\sum_{\mathbf{R}\mathbf{R}'}\sum_{ij} \tilde{t}_{ij}^{\mathbf{R}\mathbf{R}'} c_{\mathbf{R}i}^\dagger c_{\mathbf{R}'j} + \frac{1}{2}\sum_{\mathbf{R}\mathbf{R}'\mathbf{R}''\mathbf{R}'''}\sum_{ijkl} U_{ijkl}^{\mathbf{R}\mathbf{R}'\mathbf{R}''\mathbf{R}'''} c_{\mathbf{R}i}^\dagger c_{\mathbf{R}'j}^\dagger c_{\mathbf{R}''k} c_{\mathbf{R}'''l} - H_{\text{DC}} \tag{1.17}$$

where H_{DC} must be chosen to account for corrections to the double counting of terms introduced by the substitution $t_{ij}^{\mathbf{R}\mathbf{R}'} \to \tilde{t}_{ij}^{\mathbf{R}\mathbf{R}'}$. In this form, the DFT Hamiltonian is easily modified in a way which can tune the strength of electron-electron interactions whenever $U_{ijkl}^{\mathbf{R}\mathbf{R}'\mathbf{R}''\mathbf{R}'''} > 0$. Since electron-electron interactions are strongest between electrons occupying an orbital on the same atom, It is useful to take U to have a local form $U_{ijkl}^{\mathbf{R}\mathbf{R}'\mathbf{R}''\mathbf{R}'''} = U_{ijkl}^{\mathbf{R}}\delta_{\mathbf{R}\mathbf{R}'\mathbf{R}''\mathbf{R}'''}$. In this case, I will refer to the second term in (1.17) as the local Hamiltonian. A useful local Hamiltonian defined for a set of orbitals on an atom, e.g. at position $\mathbf{R}$, which I will refer to as correlated orbitals, is the Kanamori Hamiltonian [19],

$$\begin{aligned} H_{\text{loc}}^{\mathbf{R}} =& \bar{U}^{\mathbf{R}} \sum_m n_{\mathbf{R}m\uparrow} n_{\mathbf{R}m\downarrow} + U'^{\mathbf{R}} \sum_{m\neq m'} n_{\mathbf{R}m\uparrow} n_{\mathbf{R}m'\downarrow} + (U'^{\mathbf{R}} - J_H^{\mathbf{R}}) \sum_{m<m',\sigma} n_{\mathbf{R}m\sigma} n_{\mathbf{R}m'\sigma} \\ & - J_H^{\mathbf{R}} \sum_{m\neq m'} \left(c_{\mathbf{R}m\uparrow}^\dagger c_{\mathbf{R}m\downarrow} c_{\mathbf{R}m'\downarrow}^\dagger c_{\mathbf{R}m'\uparrow} - c_{\mathbf{R}m\uparrow}^\dagger c_{\mathbf{R}m\downarrow}^\dagger c_{\mathbf{R}m'\downarrow} c_{\mathbf{R}m'\uparrow} \right) \end{aligned} \tag{1.18}$$

where $n_{\mathbf{R}m\sigma} = c^{\dagger}_{\mathbf{R}m\sigma}c_{\mathbf{R}m\sigma}$, m and σ are orbital and spin indices, $\bar{U}^{\mathbf{R}}$ is the double-occupation Coulomb repulsion for electrons on the same orbital, $J_H^{\mathbf{R}}$ is referred to as Hund's coupling which enforces Hund's rules, and $U'^{\mathbf{R}} = \bar{U}^{\mathbf{R}} - 2J_H^{\mathbf{R}}$. $J_H^{\mathbf{R}}$ is often much smaller than $\bar{U}^{\mathbf{R}}$, and it is reasonable to neglect the last term. In this case, the local Hamiltonian is referred to as a density-density Hamiltonian, and the two-index matrices coupling parallel and antiparallel spins are referred to as Kanamori U and U' matrices respectively. I will refer to $\bar{U}^{\mathbf{R}}$ and $J_H^{\mathbf{R}}$ as the Hubbard-Kanamori parameters. When no ambiguity arises, $\bar{U}^{\mathbf{R}}$ is referred to as $U^{\mathbf{R}}$.

A new total energy functional called the DFT+U total energy functional can be defined as

$$E_{\text{DFT+U}} = E_{\text{DFT}}[n] + E_U[\{n^{\mathbf{R}}_{\sigma mm'}\}] - E_{\text{DC}}[\{n^{\mathbf{R}}_{\sigma mm'}\}] \tag{1.19}$$

where E_{DFT} is the DFT energy functional, E_U is a correction term incorporating Coulomb repulsion between electrons localized on an atomic orbital, and E_{DC} is a double-counting term correcting for contributions to the total energy which are counted in the calculations of E_{DFT} and E_U. The energy correction terms, E_U and E_{DC}, are functionals of the local density matrix

$$n^{\mathbf{R}}_{\sigma mm'} = \sum_{\mathbf{k}\nu} f^{\sigma}_{\mathbf{k}\nu}\langle\psi^{\sigma}_{\mathbf{k}\nu}|\phi^{\mathbf{R}}_{\sigma m}\rangle\langle\phi^{\mathbf{R}}_{\sigma m'}|\psi^{\sigma}_{\mathbf{k}\nu}\rangle \tag{1.20}$$

where $f^{\sigma}_{\mathbf{k}\nu}$ are the occupation numbers and $|\phi^{\mathbf{R}}_m\rangle$ are localized states centered around the atom site $\mathbf{R}$, for example, maximally-localized Wannier states. In this way, the additional energy cost due to strong onsite electron-electron interaction is incorporated in the next calculation of the external potential. For example, the local Coulomb repulsion functional is often taken to be the rotationally-invariant form [10],

$$E_{\text{U}}[\{n^{\mathbf{R}\sigma}_{mm'}\}] = \sum_{\mathbf{R}\sigma}\frac{1}{2}(\bar{U}^{\mathbf{R}} - J_H^{\mathbf{R}})\text{Tr}\left[n^{\mathbf{R}}_{\sigma}(1 - n^{\mathbf{R}}_{\sigma})\right] + \frac{1}{2}J_H^{\mathbf{R}}\text{Tr}\left[n^{\mathbf{R}}_{\sigma}n^{\mathbf{R}}_{-\sigma}\right] \tag{1.21}$$

An expression for the double-counting correction is often taken to be the "fully-localized limit"

$$E_{\text{DC}}[\{n^{\mathbf{R}\sigma}_{mm'}\}] = \sum_{\mathbf{R}}\frac{1}{2}\bar{U}^{\mathbf{R}}n_{\mathbf{R}}(1 - n_{\mathbf{R}}) + \sum_{\sigma}\frac{1}{2}J_H^{\mathbf{R}}n_{\mathbf{R}\sigma}(1 - n_{\mathbf{R}\sigma}) \tag{1.22}$$

1.2.4 Dynamical Mean-Field Theory

Dynamical mean-field theory (DMFT) is most simply understood in its application to the one-band Hubbard model with only nearest-neighbour hopping,

$$H = \sum_{\langle ij\rangle\sigma} t_{ij}(c^\dagger_{i\sigma}c_{j\sigma} + h.c.) + U\sum_i c^\dagger_{i\uparrow}c_{i\uparrow}c^\dagger_{i\downarrow}c_{i\downarrow}. \tag{1.23}$$

In DMFT, the self energy relating the non-interacting Green's function with the interacting Green's function is self-consistently mapped to the self-energy of an auxiliary Anderson impurity model (AIM). It was shown that this approximation is exact in the limit of infinite lattice dimensions. DMFT is "dynamical" in the sense that it is developed in the Lagrangian formalism in contrast with the Weiss mean-field theory of classical spin models in the Hamiltonian formalism. The AIM Hamiltonian for one orbital coupled to a bath of non-interacting electrons is

$$\mathcal{H} = \sum_{\mathbf{k}\sigma}\epsilon_{\mathbf{k}\sigma}c^\dagger_{\mathbf{k}\sigma}c_{\mathbf{k}\sigma} + \sum_{\mathbf{k}\sigma}V_{\mathbf{k}\sigma}(c^\dagger_{\mathbf{k}\sigma}d_\sigma + \text{h.c.}) + \epsilon_d\sum_\sigma d^\dagger_\sigma d_\sigma + Ud^\dagger_\uparrow d_\uparrow d^\dagger_\downarrow d_\downarrow, \tag{1.24}$$

where $c_{\mathbf{k}\sigma}$ are annihilation operators for the bath electrons and $d_{i\sigma}$ are annihilation operators for the impurity electrons. The corresponding action is

$$S_{\text{AIM}} = -\int_0^\beta d\tau\int_0^\beta d\tau'\sum_\sigma \psi^*_\sigma(\tau)\mathcal{G}^{-1}_\sigma(\tau-\tau')\psi_\sigma(\tau') + \int_0^\beta d\tau\ U\ \psi^*_\uparrow(\tau)\psi_\uparrow(\tau)\psi^*_\downarrow(\tau)\psi_\downarrow(\tau) \tag{1.25}$$

where ψ_σ and ψ^*_σ are independent Grassmann variables,

$$\mathcal{G}_\sigma(i\omega_n) = [i\omega_n + \epsilon_d - \Delta_\sigma(i\omega_n)]^{-1} \tag{1.26}$$

is the Fourier-transformed non-interacting impurity Green's function and,

$$\Delta_\sigma(i\omega_n) = \sum_k \frac{|V_{\mathbf{k}\sigma}|^2}{i\omega_n - \epsilon_{\mathbf{k}\sigma}} \tag{1.27}$$

is referred to as the hybridization function. Here ω_n are fermionic Matsubara frequencies, $\omega_n = (2n+1)\pi/\beta$ for integer n, as required by the exchange antisymmetry of fermions.

Starting from an initial guess for $\Delta_\sigma(i\omega_n)$, the interacting Green's function for the auxiliary AIM can be calculated using an impurity solver such as quantum Monte Carlo (QMC)

$$G_\sigma(\tau) = \langle\mathcal{T}d_\sigma(\tau)d_\sigma(0)\rangle_{S_{\text{AIM}}} \tag{1.28}$$

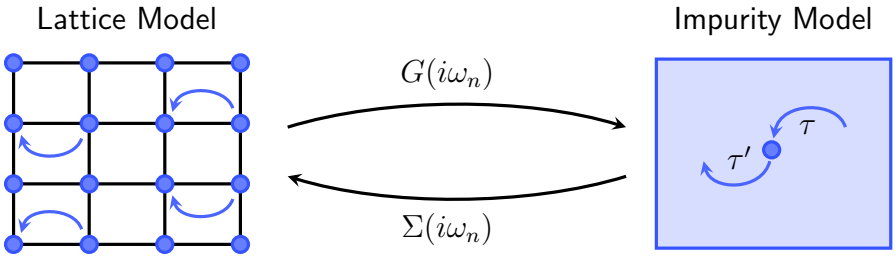

Figure 1.2: Depiction of the DMFT self-consistent mapping procedure.

The self energy can then be calculated through the Dyson equation

$$\Sigma_\sigma(i\omega_n) = \mathcal{G}_\sigma^{-1}(i\omega_n) - G_\sigma^{-1}(i\omega_n) \tag{1.29}$$

Now this self energy is used to approximate the self energy of the lattice model $\Sigma_\sigma^{latt}(\mathbf{k},\omega) \to \Sigma_\sigma(\omega)$. From this, the local lattice Green's function is then computed

$$G_\sigma(i\omega_n) = \frac{V}{(2\pi)^3}\int_{\mathrm{BZ}} \left[i\omega_n - \epsilon_{\mathbf{k}\sigma} + \mu - \Sigma_\sigma(i\omega_n)\right]^{-1} \tag{1.30}$$

This Green's function is equated to the interacting Green's function for the impurity model, and a new non-interacting Green's function for the impurity model is obtained from the Dyson equation

$$\mathcal{G}_\sigma(i\omega_n) = \left(G_\sigma(i\omega_n)^{-1} + \Sigma_\sigma(i\omega_n)\right)^{-1} \tag{1.31}$$

This procedure is repeated until convergence of the hybridization function. Paramagnetism can be enforced by setting $\Sigma_\sigma = (\Sigma_\uparrow + \Sigma_\downarrow)/2$ before the local lattice Green's function is computed in each iteration.

Once the Green's function for the auxiliary impurity system has been obtained self-consistently, the spectral density can be obtained from analytic continuation

$$A(\omega) = -\frac{1}{\pi}\mathrm{Im}\left[G(\omega + i0^+)\right] \tag{1.32}$$

The quasiparticle renormalization factor and mass enhancement factor of bath electrons due to the inclusion of the impurity orbital are obtained from the impurity self energy as

$$m^*/m^{\mathrm{DFT}} = Z^{-1} = 1 - \left.\frac{\partial \mathrm{Im}\Sigma(i\omega_n)}{\partial\omega_n}\right|_{\omega_n\to 0^+}. \tag{1.33}$$

This is typically interpreted as a measure of the strength of electronic correlations since the self energy is zero for independent Bloch states, so that m^*/m^{DFT} is

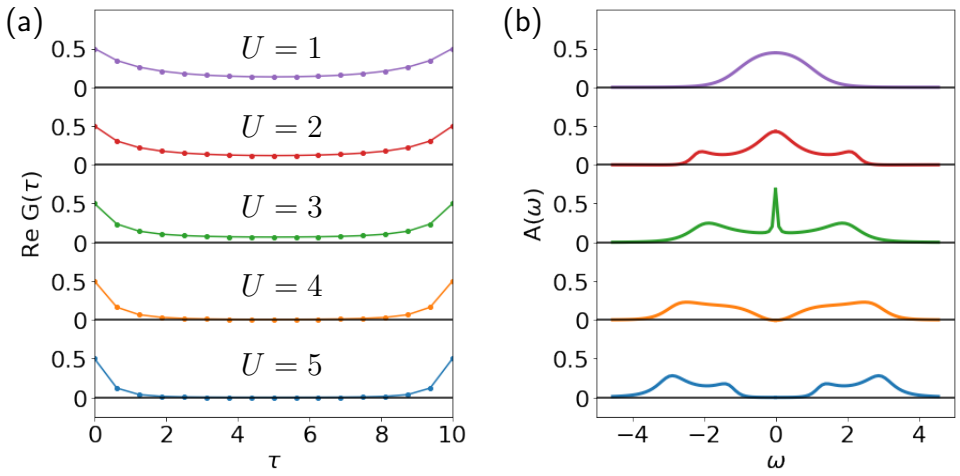

Figure 1.3: (a) Imaginary-time Green's function and (b) spectral density of the auxiliary impurity model obtained from DMFT for the Hubbard model with a semi-circular density of states and paramagnetism enforced. A Mott-insulator transition occurs for a value of U between 3 and 4 in units of $\sqrt{2}t$.

one, and m^*/m^{DFT} diverges at a Mott-insulator transition. Since the Matsubara frequencies take discrete values at finite temperature, the self-energy derivative is approximated by $(\Sigma(i\omega_2) - \Sigma(i\omega_1))/(\omega_2 - \omega_1)$ where ω_1 and ω_2 are the first two positive Matsubara frequencies, and the derivative is only exact in the zero temperature limit. It is therefore easy to distinguish between a metallic or insulating state by observing if the imaginary part of the Matsubara-frequency self energy diverges as $\omega_n \to 0^+$, implying the imaginary part of the lattice Green's function becomes zero as $\omega_n \to 0^+$, without the need for analytic continuation. Alternatively, one can check if $\mathrm{Re}\,[G(\beta/2)]$, which is proportional to the spectral density at the chemical potential, is non-zero.

As an example, the imaginary-time Green's function and spectral density for the Hubbard model with semi-circular density of states, which corresponds with the model defined for the Bethe lattice with only nearest-neighbour hopping in the limit of infinite coordination, is calculated and plotted in Fig. 1.3. The Green's function is calculated by exact enumeration of auxiliary Ising spin configurations in the Hubbard-Stratonovich transformation of terms in the Trotter decomposition of the partition function discretized over 16 evenly spaced imaginary-time steps at $\beta = 10/\sqrt{2}t$ as is done in, e.g. Ref. [12]. The spectral density is then obtained through analytical continuation using Padé approximants calculated by the method given in Ref. [47].

1.2.5 DFT+DMFT

Similarly to DFT+U, the results of a DFT calculation can be supplemented with DMFT as a means of incorporating strong electron-electron interactions neglected in the DFT calculation. The DFT Green's function is

$$G^0_{\mu\nu}(\mathbf{k}, i\omega_n) = \left[i\omega_n + \mu - \epsilon_{\nu\mathbf{k}}\right]^{-1} \delta_{\mu\nu} \tag{1.34}$$

Then the non-interacting Green's function for a multi-orbital impurity model is taken to be

$$G^0_{mn}(i\omega_n) = \frac{V}{(2\pi)^3} \int_{\mathrm{BZ}} \sum_{\mu\nu} P_{m\mu}(\mathbf{k}) G^0_{\mu\nu}(\mathbf{k}, i\omega_n) P^*_{\nu n}(\mathbf{k}) \tag{1.35}$$

where $P_{n\nu}(\mathbf{k}) = |\phi_n\rangle\langle\psi_{\nu\mathbf{k}}|$ are projectors from the KS band basis to a local Wannier-orbital basis. The projection of quantities from (to) the KS basis to (from) the Wannier basis is referred to as downfolding (upfolding). The interacting Green's function for the impurity model is then computed using an impurity solver such as quantum Monte Carlo. The new self energy is then

$$\Sigma_{mn}(i\omega_n) = G^0_{mn}(i\omega_n)^{-1} - G_{mn}(i\omega_n)^{-1} - \Sigma^{\mathrm{DC}} \tag{1.36}$$

where the Σ^{DC} term is included here to subtract the double counting of electron-electron interactions included in both of the DMFT and DFT calculations. The lattice self energy in the KS basis is then obtained through upfolding,

$$\Sigma_{\mu\nu}(\mathbf{k}, i\omega_n) = \sum_{mn} P^*_{\mu m}(\mathbf{k}) \Sigma_{mn}(i\omega_n) P_{n\nu}(\mathbf{k}). \tag{1.37}$$

Then the lattice Green's function is computed as

$$G^{\mathrm{latt}}_{\mu\nu}(\mathbf{k}, i\omega_n) = \left[i\omega_n + \mu - \epsilon_{\nu\mathbf{k}}\delta_{\mu\nu} - \Sigma_{\mu\nu}(\mathbf{k}, i\omega_n)\right]^{-1} \tag{1.38}$$

and the local lattice Green's function is obtained through downfolding

$$G^{\mathrm{loc}}_{mn}(i\omega_n) = \frac{V}{(2\pi)^3} \int_{\mathrm{BZ}} \sum_{\mu\nu} P_{m\mu}(\mathbf{k}) G^{\mathrm{latt}}_{\mu\nu}(\mathbf{k}, i\omega_n) P^*_{\nu n}(\mathbf{k}) \tag{1.39}$$

Then the non-interacting Green's function for the impurity model is equated to

$$G^0_{mn}(i\omega_n) = \left[G^{\mathrm{loc}}_{mn}(i\omega_n)^{-1} + \Sigma_{mn}(i\omega_n)\right]^{-1} \tag{1.40}$$

This can be used to start a new DMFT iteration and repeated until convergence of the hybridization function, or the charge density can be computed from the lattice Green's function as

$$n(\mathbf{r}) = \frac{1}{\beta} \sum_n \langle \mathbf{r} | G^{\mathrm{latt}}_{\mu\nu}(\mathbf{k}, i\omega_n) | \mathbf{r} \rangle \tag{1.41}$$

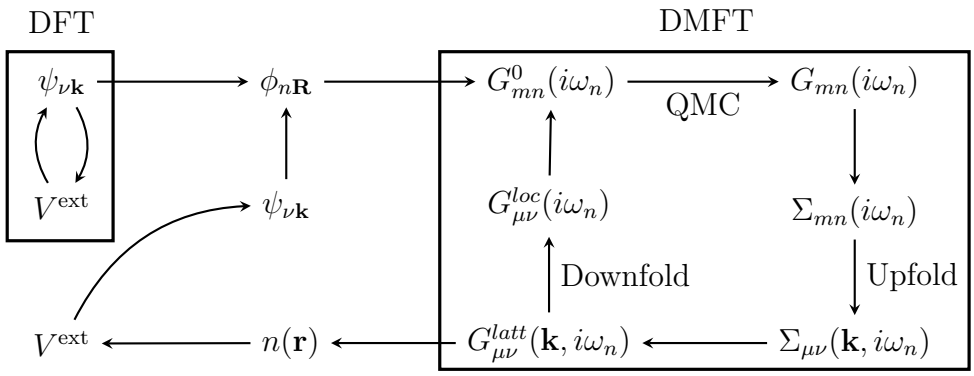

Figure 1.4: Diagram depicting the charge-self-consistent DFT+DMFT procedure.

This can then be used to define a new KS potential, and subsequently compute new KS states and Wannier projectors. These are then used to start a new DMFT iteration and the procedure is repeated until convergence of the charge density. Convergence of the hybridization function without calculation of an updated KS potential is referred to as one-shot (OS) DFT+DMFT. Convergence of both the hybridization function and charge density is referred to as fully charge self-consistent (CSC) DFT+DMFT. The DFT+DMFT self-consistency procedure is summarized by the diagram in Fig. 1.4.

Once full charge self consistency has been achieved, the spectral function can be obtained from upfolding the analytically-continued real-frequency impurity self energy

$$A(\mathbf{k},\omega) = -\frac{1}{\pi}\text{Tr}\left(\text{Im}\left[G^{\text{latt}}_{\mu\nu}(\mathbf{k},\omega + i0^+)\right]\right) \tag{1.42}$$

As an example, the DFT+DMFT impurity Green's function, self energy, and spectral function for $SrVO_3$ are plotted in Fig. 1.5. A density-density interaction Hamiltonian was used with Kanamori U and U' matrices constructed using $\bar{U} =$ 4eV and $J_H = 0.7$eV. The double-counting correction as given in Ref. [17] suitable for Kanamori Hamiltonians was used. The correlated subsystem was taken to be the Wannier-projected t_{2g} orbitals. The Wannier projectors were constructed using the method given in Ref. [3] as implemented in the dmftproj program associated with the TRIQS/DFTTools library [1]. A wide energy window of [-8.5,7.5] eV was used in the construction of the projectors. The self energy was analytically continued by the maximum-entropy method with hyperparameter, α, determined by the line-fit intersection method as implemented in the maxent library associated with the TRIQS library [23].

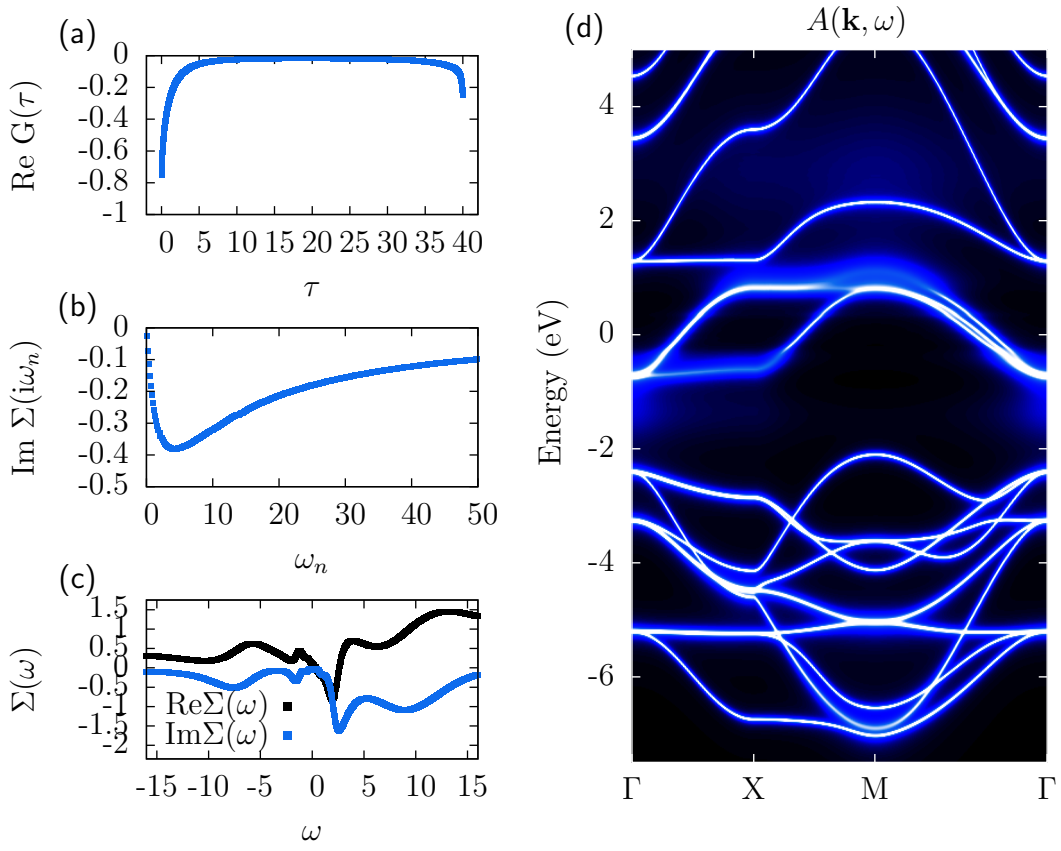

Figure 1.5: (a) Imaginary-time impurity Green's function and (b) Matsubara impurity self energy for the V-t_{2g} orbital of $SrVO_3$ obtained from DFT+DMFT. (c) Analytically continued real-frequency impurity self energy. (d) DFT+DMFT spectral function.

1.2.6 Topological Classification and Surface States

For centrosymmetric materials, it was shown by Fu and Kane that the Z_2 topological invariant characterizing band structure topology can be simply calculated through a parity product of occupied orbitals evaluated at 8 time-reversal invariant momenta (TRIM) [11]. The parity of each KS orbital is calculated at the TRIM for each occupied valence band is used to form a parity product. That is,

$$\delta_i = \prod_{\nu} \zeta_\nu(\Lambda_i) \tag{1.43}$$

is referred to as a parity product at the TRIM, Λ_i, where ζ_ν is the parity of the Kramers-degenerate KS orbital ψ^σ_ν, and the product is calculated over all valence

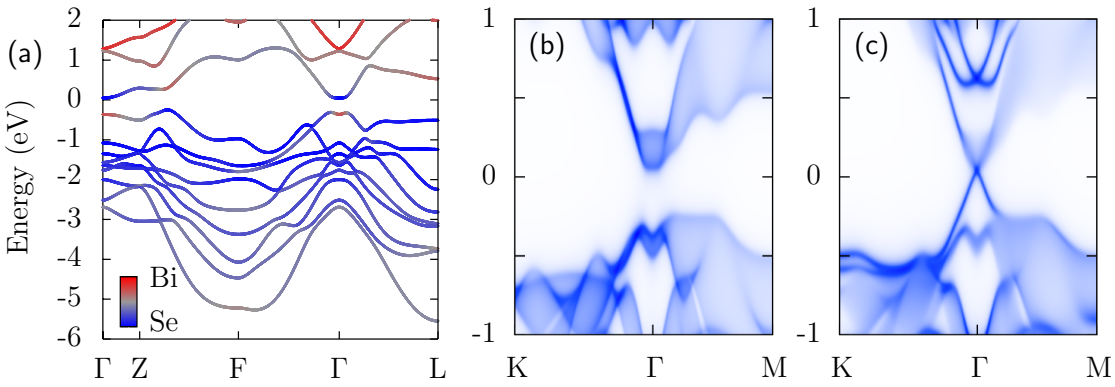

Figure 1.6: DFT band structure (a), bulk (001)-projected states (b), and (001) surface states of Bi_2Se_3 (c). The bands in (a) are coloured according to the projection of maximally-localized Wannier functions centered on Bi (blue) and Se (red) atoms.

orbitals. The TRIM are typically taken to be $\Lambda_{(n_1,n_2,n_3)} = n_1\frac{1}{2}\mathbf{b}_1 + n_2\frac{1}{2}\mathbf{b}_2 + n_3\frac{1}{2}\mathbf{b}_3$ for each $n_i \in \{0,1\}$. Then weak topological indices may be defined in terms of the total parity product over time-reversal-invariant planes,

$$(-1)^{\nu_1} = \delta_{(1,0,0)}\delta_{(1,1,0)}\delta_{(1,0,1)}\delta_{(1,1,1)} \tag{1.44}$$
$$(-1)^{\nu_2} = \delta_{(0,1,0)}\delta_{(1,1,0)}\delta_{(0,1,1)}\delta_{(1,1,1)} \tag{1.45}$$
$$(-1)^{\nu_3} = \delta_{(0,0,1)}\delta_{(1,0,1)}\delta_{(0,1,1)}\delta_{(1,1,1)} \tag{1.46}$$

and the strong topological invariant is defined as the total parity product over every TRIM. The Z_2 index is a combination of each of these numbers and is denoted by $Z_2 = (\nu_0;\nu_1,\nu_2,\nu_3)$. There are three additional time-reversal-invariant planes for which weak topological invariants can be defined. For example, $(-1)^{\nu_4} = \delta_{(0,0,0)}\delta_{(0,1,0)}\delta_{(0,0,1)}\delta_{(0,1,1)}$. However, this is redundant since ν_4 is related to ν_0 and ν_1 through $(-1)^{\nu_0} = (-1)^{\nu_1}(-1)^{\nu_4}$.

The existence of a topologically non-trivial band separated by a direct gap from a topologically trivial band implies the existence of a topological surface state band closing the gap. This means that a material may be insulating in the bulk consistent with band theory, while the surface may be conductive. An iterative method, e.g. as defined in Ref. [37], may be used to calculate the surface-state spectral function from the DFT Green's function for a semi-infinite system.

As an example, Bi_2Se_3 is a semiconductor in the bulk, but the topological nature of the highest valence band, with Z_2 indices $(\nu_0;\nu_1,\nu_2,\nu_3) = (1;0,0,0)$, forces conduction on the surface in the form of a linear Dirac-like dispersion. I have plotted the Wannier-orbital character of the DFT bands along with the bulk

band	rep.				parity prod.			
#	Γ (D_{3d})	L (C_{2h})	F (C_{2h})	Z (D_{3d})	δ_Γ	δ_L	δ_F	δ_Z
14	Γ_4^+	$\Gamma_3^- \oplus \Gamma_4^-$	$\Gamma_3^- \oplus \Gamma_4^-$	Γ_4^+	-1	1	1	1
13	$\Gamma_5^- \oplus \Gamma_6^-$	$\Gamma_3^- \oplus \Gamma_4^-$	$\Gamma_3^- \oplus \Gamma_4^-$	$\Gamma_5^- \oplus \Gamma_6^-$	-1	-1	-1	1
12	Γ_4^-	$\Gamma_3^- \oplus \Gamma_4^-$	$\Gamma_3^+ \oplus \Gamma_4^+$	$\Gamma_5^+ \oplus \Gamma_6^+$	1	1	1	-1
11	$\Gamma_5^- \oplus \Gamma_6^-$	$\Gamma_3^+ \oplus \Gamma_4^+$	$\Gamma_3^- \oplus \Gamma_4^-$	Γ_4^-	-1	-1	1	-1
10	$\Gamma_5^+ \oplus \Gamma_6^+$	$\Gamma_3^- \oplus \Gamma_4^-$	$\Gamma_3^+ \oplus \Gamma_4^+$	Γ_4^-	1	-1	-1	1
9	Γ_4^-	$\Gamma_3^+ \oplus \Gamma_4^+$	$\Gamma_3^- \oplus \Gamma_4^-$	$\Gamma_5^- \oplus \Gamma_6^-$	1	1	-1	-1
8	Γ_4^+	$\Gamma_3^+ \oplus \Gamma_4^+$	$\Gamma_3^- \oplus \Gamma_4^-$	Γ_4^+	-1	1	1	1
7	Γ_4^+	$\Gamma_3^- \oplus \Gamma_4^-$	$\Gamma_3^+ \oplus \Gamma_4^+$	Γ_4^-	-1	1	-1	1
6	Γ_4^-	$\Gamma_3^- \oplus \Gamma_4^-$	$\Gamma_3^- \oplus \Gamma_4^-$	Γ_4^-	-1	-1	-1	-1
5	Γ_4^+	$\Gamma_3^+ \oplus \Gamma_4^+$	$\Gamma_3^+ \oplus \Gamma_4^+$	Γ_4^+	1	1	1	1
4	Γ_4^-	$\Gamma_3^- \oplus \Gamma_4^-$	$\Gamma_3^- \oplus \Gamma_4^-$	Γ_4^-	1	1	1	1
3	Γ_4^+	$\Gamma_3^+ \oplus \Gamma_4^+$	$\Gamma_3^+ \oplus \Gamma_4^+$	Γ_4^+	-1	-1	-1	-1
2	Γ_4^-	$\Gamma_3^- \oplus \Gamma_4^-$	$\Gamma_3^+ \oplus \Gamma_4^+$	Γ_4^-	-1	-1	-1	-1
1	Γ_4^+	$\Gamma_3^+ \oplus \Gamma_4^+$	$\Gamma_3^- \oplus \Gamma_4^-$	Γ_4^+	1	1	-1	1

Table 1.1: Orbital symmetries for the highest 14 valence bands at TRIM as well as the corresponding parity products.

projected states and surface state spectral function in Fig. 1.6. I have used the iterative method of Ref. [37] as implemented in the WannierTools program [49] to compute the surface states. It can be seen in Fig. 1.6 that band theory predicts Bi_2Se_3 to be an insulator for an infinite periodic system. However, conducting surface states in the form of a Dirac cone are present in a semi-infinite system. In this case, band inversion induced by spin-orbit coupling changes the parity of the band at the Γ point leading to non-trivial band topology. The parity products at TRIM for the highest 14 valence bands are given in Table 1.1 which implies the topologically non-trivial Z_2 index, $Z_2 = (1; 0, 0, 0)$.

1.2.7 Electron-Phonon Coupling and Superconductivity

The electron-phonon vertex, $g^\nu_{mn}(\mathbf{k}, \mathbf{k}') = \langle \psi_{m\mathbf{k}+\mathbf{k}'} | \partial_{\mathbf{k}'\nu} V | \psi_{n\mathbf{k}} \rangle$, which plays a central role in the Eliashberg theory of superconductivity can be calculated using maximally-localized Wannier functions obtained from the DFT Bloch states, $|\psi_{n\mathbf{k}}\rangle$, as described in Section 1.2.2, as well as force constants obtained from density functional perturbation theory [14]. Eliashberg theory can be viewed as a dynamical mean-field extension of the conventional BCS theory such that the frequency dependence of the superconducting gap function is considered in the gap equations.

The approximate Eliashberg equations for the anisotropic gap function, which are derived from a more general set of equations for the superconducting order parameter, are

$$Z(\mathbf{k}, i\omega_n) = 1 + \frac{\pi T}{\omega_n} \sum_{\mathbf{k}'n'} \frac{\delta(\epsilon_{\mathbf{k}'} - \epsilon_F)}{N(\epsilon_F)} \frac{\omega_{n'}}{\sqrt{\omega_n^2 + \Delta(\mathbf{k}', i\omega_{n'})}} \lambda(\mathbf{k}, \mathbf{k}', i\omega_n - i\omega_{n'}) \tag{1.47}$$

$$Z(\mathbf{k}, i\omega_n)\Delta(\mathbf{k}, i\omega_n) = \pi T \sum_{\mathbf{k}n'} \frac{\delta(\epsilon_{\mathbf{k}'} - \epsilon_F)}{N(\epsilon_F)} \frac{\Delta(\mathbf{k}', i\omega_{n'})}{\sqrt{\omega_n^2 + \Delta(\mathbf{k}', i\omega_{n'})}} \left[\lambda(\mathbf{k}, \mathbf{k}', i\omega_n - i\omega_{n'}) - \mu^*\right] \tag{1.48}$$

which are equivalent to the BCS gap equations in the limit of frequency-independent electron-phonon coupling, λ, and gap function. The electron-phonon coupling is given by

$$\lambda(\mathbf{k}, \mathbf{k}', i\omega_n) = \int_0^\infty d\omega \frac{2\omega}{\omega_n^2 + \omega^2} \alpha^2_{\mathbf{k}\mathbf{k}'} F(\omega) \tag{1.49}$$

where $\alpha^2_{\mathbf{k}\mathbf{k}'}F$ is referred to as the Eliashberg spectral function and is equal to,

$$\alpha^2_{\mathbf{k}\mathbf{k}'} F(\omega) = \frac{1}{N(\epsilon_F)} \sum_{mn\nu} |g^\nu_{mn}(\mathbf{k}, \mathbf{k}')|^2 \delta(\omega - \omega_{\mathbf{k}-\mathbf{k}'\nu}) \delta(\epsilon_{n\mathbf{k}} - \epsilon_F) \delta(\epsilon_{m\mathbf{k}+\mathbf{k}'} - \epsilon_F) \tag{1.50}$$

The isotropic Eliashberg spectral function is defined as

$$\alpha^2 F(\omega) = \frac{V}{(2\pi)^3} \int_{BZ} d^3k \frac{V}{(2\pi)^3} \int_{BZ} d^3k' \alpha^2_{\mathbf{k}\mathbf{k}'} F(\omega) \tag{1.51}$$

and the strength of electron-phonon coupling is typically quantified by

$$\lambda = \frac{V}{(2\pi)^3} \int_{BZ} d^3k \frac{V}{(2\pi)^3} \int_{BZ} d^3k' \lambda(\mathbf{k}, \mathbf{k}', 0) = 2 \int_0^\infty d\omega \frac{d\omega}{\omega} \alpha^2 F(\omega) \tag{1.52}$$

The phonon density of states is referred to as $F(\omega)$. After solving the Eliashberg equations for the gap function, the real-frequency gap function can be obtained by analytic continuation. For example, by using Padé approximants.

As an example, the anisotropic Eliashberg equations are solved for the multi-gapped superconductor, MgB_2. The results can be seen in Fig. 1.7. While the transition temperatures is significantly overestimated when compared with the experimental value [6], Eliashberg theory is able to capture the expected two-gap behaviour of the superconducting state. The superconducting critical temperature may be computed more accurately by incorporating the superconducting order parameter in the DFT exchange-correlation functional [38].

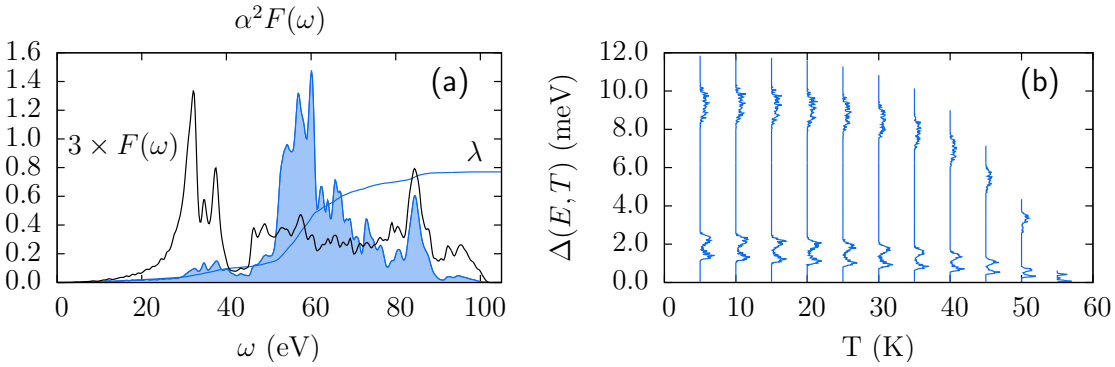

Figure 1.7: (a) Phonon density of states (black), Eliashberg spectral function (blue), and cumulative electron-phonon coupling (blue line) for MgB2. The phonon density of states is multiplied by a factor of 3 for better visualization. (b) Gap function for MgB_2 obtained from solution of the anisotropic Eliashberg equations.

Chapter 2

Argument for a Non-Unitary Triplet-Pairing State in the Time-Reversal-Symmetry Breaking Superconductor TaRuSi and Comparison with TaReSi

2.1 Background and Experimental Observations

To preface this chapter, I will first state some general facts about the superconducting gap function based on symmetry analysis. Most of which are given, for example, in Ref. [44]. A general form of the superconducting gap function for a singlet-pairing state satisfying the parity antisymmetry condition, $\Delta(\mathbf{k}) = -\Delta(-\mathbf{k})^T$ can be written as

$$\Delta(\mathbf{k}) = \Delta_0(\mathbf{k}) i\sigma_y \tag{2.1}$$

where Δ_0 is an even function of $\mathbf{k}$. For a triplet-pairing state satisfying the parity symmetry condition, $\Delta(\mathbf{k}) = \Delta(-\mathbf{k})^T$, the gap function has the general form,

$$\Delta(\mathbf{k}) = (\mathbf{d}(\mathbf{k}) \cdot \sigma) i\sigma_y \tag{2.2}$$

For non-centrosymmetric materials, the gap function has no parity requirement, and the general form allowing for a mixed-parity state is

$$\Delta(\mathbf{k}) = \Delta_0(\mathbf{k}) i\sigma_y + (\mathbf{d}(\mathbf{k}) \cdot \sigma) i\sigma_y \tag{2.3}$$

where $\mathbf{d}$ is an odd function of $\mathbf{k}$. For a triplet state, $\Delta(\mathbf{k})$ is referred to as unitary when $\Delta(\mathbf{k})\Delta(\mathbf{k})^T$ is proportional to the identity. Otherwise, it is referred to as non-unitary, which is only possible when $d(\mathbf{k}) \neq d^*(\mathbf{k})$. The gap function transforms under crystallographic point group transformations as $\Delta_0(\mathbf{k}) \rightarrow \Delta_0(D_{G_c}(g)\mathbf{k})$, and, $\mathbf{d}(\mathbf{k}) \rightarrow \mathbf{d}(D_{G_c}(g)\mathbf{k})$, where $D_{G_c}(g)$ is a matrix corresponding with the group operation, $g \in G_c$ for the point group G_c. Assuming no spin-orbit coupling, the symmetry group of the gap function is $G = G_c \times SO(3)$. Then, on the basis of Landau theory, the free energy may be written as a power series of all symmetry-allowed order parameters, and therefore the gap function realized in a superconductor is expected to have the symmetry of the irreducible representation (irrep), Γ, of G which minimizes the free energy. That is, for a d-dimensional irrep, the ground-state gap function is

$$\Delta(\mathbf{k}) = \sum_{n=1}^{d} c_n \Delta_n^{\Gamma}(\mathbf{k}) \tag{2.4}$$

where $\Delta_n^{\Gamma}(\mathbf{k})$ correspond with the basis functions of Γ, and c_n are complex coefficients transforming as $c_n \rightarrow c_n^*$ under time reversal.

Applying time reversal to the singlet- and triplet-pairing states, assuming no spin-orbit coupling, has the effects $\Delta_0(\mathbf{k}) \rightarrow \Delta_0^*(-\mathbf{k})$, and, $\mathbf{d}(\mathbf{k}) \rightarrow -\mathbf{d}^*(-\mathbf{k})$. Therefore, time-reversal symmetry (TRS) breaking may be possible if the gap function minimizing the free energy satisfies one of the following. It has symmetry of an irrep of two dimensions or higher, it is in a coexisting phase stabilizing two or more gap functions corresponding with different irreps, or it describes a non-unitary triplet state. In non-centrosymmetric materials, the gap function is not required to satisfy a parity condition enforced by the crystallographic symmetry. This allows for the possibility of a mixed singlet-triplet superconducting state, as well as the existence of antisymmetric spin-orbit coupling (ASOC).

The compounds TaRuSi and TaReSi, which I will collectively refer to as TaXSi, are the main subject of this chapter. They both crystallize in a non-centrosymmetric orthorhombic structure with low-symmetry C_{2v} point group. It is very similar to the crystal structure of $LaNiC_2$, which is also orthorhombic with C_{2v} point group. The similarity between TaXSi and $LaNiC_2$ is worth emphasizing because the superconducting state of $LaNiC_2$ was found to break TRS in muon spin-relaxation (μ-SR) experiments, and symmetry analysis of the C_{2v} point group dictates that the superconducting state should be a non-unitary triplet state. I will claim that the same conclusion should be true for TaRuSi, given recent μ-SR experiments also show evidence of TRS breaking in the superconducting state of TaRuSi [43, 42].

The argument for a non-unitary triplet state in the superconducting state of $LaNiC_2$, which also applies to the TRS broken superconducting state of TaRuSi,

Irrep (C_{2v})	singlet $\Delta_0(\mathbf{k})$	unit. triplet $\mathbf{d}(\mathbf{k})$	non-unit. triplet $\mathbf{d}(\mathbf{k})$	mixed-parity $\Delta_0(\mathbf{k})$	mixed-parity $\mathbf{d}(\mathbf{k})$
A_1	1	$(0,0,1)Z$	$(1,i,0)Z$	A	$(BY, CX, DXYZ)$
A_2	XY	$(0,0,1)XYZ$	$(1,i,0)XYZ$	AXY	(BX, CY, DZ)
B_1	XZ	$(0,0,1)X$	(1,i,0)X	AXZ	$(BXYZ, CZ, DY)$
B_2	YZ	$(0,0,1)Y$	(1,i,0)Y	AYZ	$(BZ, CXYZ, DX)$

Table 2.1: Basis functions of the symmetry-allowed superconducting states corresponding with the irreps of C_{2v}.

is as follows. In the limit of negligible spin-orbit coupling, the symmetry group of the superconducting gap function is $C_{2v} \times SO(3)$. The symmetry-allowed basis functions of which are the singlet, unitary triplet, and non-unitary triplet states given in Table 2.1. In writing Table 2.1, I have followed the conventions of Ref. [34]. Since each irrep is one-dimensional, the only possible states that break TRS when SOC is neglected are the non-unitary triplet states with the property $\mathbf{d}(\mathbf{k}) \neq \mathbf{d}^*(\mathbf{k})$. When SOC is considered non-negligible, the superconducting state corresponds with the basis functions of the mixed-parity states given in Table 2.1. None of which break time-reversal symmetry.

The question of whether spin-orbit coupling may be considered weak or not can be addressed by analysis of density functional theory calculations. A common procedure is to perform two separate DFT calculations, one with the inclusion of spin-orbit coupling and one without. Since we are considering non-magnetic materials, the DFT bands obtained in the case of no spin orbit coupling are two-fold degenerate due to spin degeneracy. Spin-orbit coupling may then split the spin degeneracy of the bands. The amount of band splitting for bands near the Fermi energy, often referred to as E_{ASOC}, can then be used as a measure of the strength of spin-orbit coupling present in the material. E_{ASOC} is therefore not well defined, but is often taken to be an average of the band splitting or within a range of the maximum and minimum band splitting. This procedure has been carried out for many systems, the value of E_{ASOC} for many of which is tabulated in, for example, Ref. [45]. The value of E_{ASOC} for $LaNiC_2$ in particular was estimated to be 42 meV [15].

2.2 Electronic Structure

DFT calculations were performed using Quantum Espresso [13]. The generalized-gradient approximation [33] was used to approximate the exchange-correlation functional. A 6×6×6 Monkhorst-Pack **k**-point grid was used to sample the Bril-

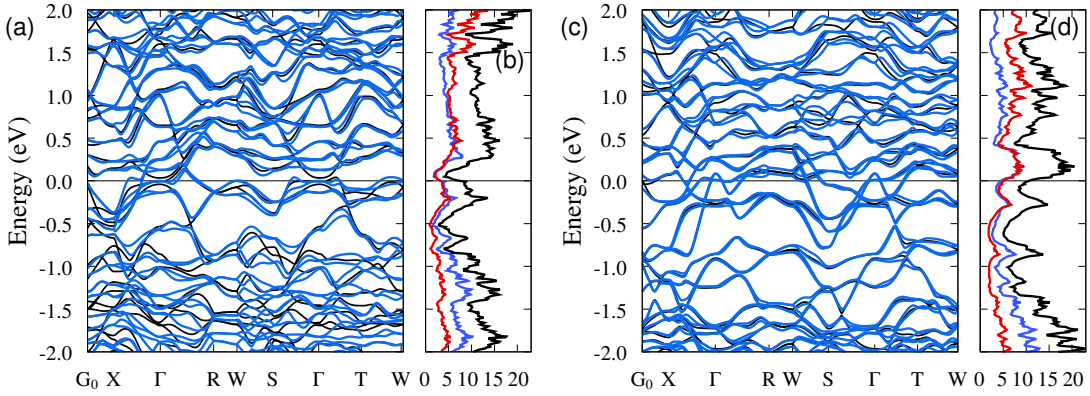

Figure 2.1: (a) TaReSi band structure with SOC (blue) and without SOC (black). (b) TaReSi total (black), Re-projected (blue), and Ta-projected (red) density of states with SOC. (c-d) The same quantities were calculated for TaRuSi as in (a-b), respectively. Figure reproduced from Ref. [43].

louin zone in the DFT self-consistency cycle, while the density of states, Fermi energy, and Fermi surfaces were computed using a dense 24×24×24 **k**-point grid. All results were found to be well converged when a kinetic energy cutoff of 100 Ry for the wavefunctions and 400 Ry for the charge density were used. Convergence with respect to varying the size of the **k**-point grid was also checked. Projector augmented-wave pseudopotentials with nonlinear core correction, as provided in the PSlibrary associated with Quantum Espresso, were used. The unit cell and atomic positions are relaxed until forces on each atom are less than 10^{-3} Ry/Bohr and pressure on the unit cell was less than 0.5 kbar. The experimentally determined lattice constants [32] were used as a starting condition for the relaxation. I have also tried initializing the relaxation procedure using lattice constants measured in an older XRD experiment [46] with no difference in the final relaxed lattice constants. The resulting lattice constants are $a = 7.02$ Å, $b = 11.56$ Å, and $c = 6.70$ Å for TaReSi, and $a = 7.30$ Å, $b = 11.20$ Å, and $c = 6.51$ Å for TaRuSi are in agreement with the values reported in Ref. [32] which were measured using X-ray diffraction at room temperature.

The resulting band structure with and without the inclusion of SOC for both materials is shown in Fig. 2.1 along with the corresponding atom-projected density of states. Multiple bands crossing the Fermi energy can be easily seen in both systems. The bands corresponding with the TaReSi system are significantly altered by the inclusion of SOC, while the bands corresponding with the TaRuSi system are only slightly altered by the inclusion of SOC.

The spin-orbit coupling (SOC) energy scale, E_{ASOC}, is often estimated in DFT

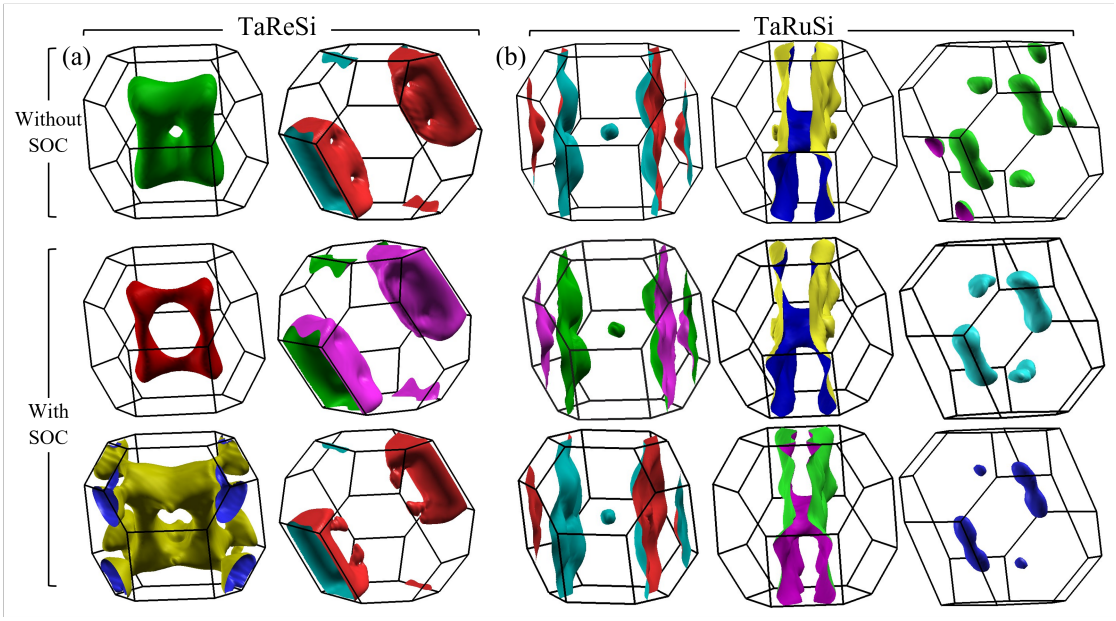

Figure 2.2: Fermi surface plots for TaReSi and TaRuSi with and without SOC. The effect of SOC on splitting the Fermi surfaces can be seen by comparing the top row to the bottom two rows in the case of (a) TaReSi and (b) TaRuSi. Fermi surface sections plotted in (a) differ significantly between the top and bottom rows, indicating the strong effect of SOC on Fermi surface splitting for TaReSi. However, the Fermi surface sections plotted in the top row of (b) are close to those of the bottom rows, indicating a weak effect of SOC on Fermi surface splitting for TaRuSi. Figure reproduced from Ref. [43].

calculations by the amount of band splitting resulting from a DFT calculation including SOC in comparison with a DFT calculation without SOC [45]. It can be seen in Fig. 2.1 that the DFT band structure is significantly affected by the inclusion of SOC in TaReSi, while the band splitting is much smaller in TaRuSi. The band splitting for **k**-points plotted in Fig. 2.1 is estimated to be at most about 50 meV for TaRuSi and well over 100 meV for many bands near the Fermi surface for TaReSi. The Fermi surfaces for each system with and without SOC are plotted in Fig. 2.2. Similar to the band splitting seen in Fig. 2.1, it can be seen in Fig. 2.2 that the splitting of the Fermi surfaces is much more pronounced in TaReSi when compared with TaRuSi. This gives an indication that the effect of SOC is fairly weak in TaRuSi in comparison with TaReSi.

In order to compare of the strength of E_{ASOC} for TaXSi with other superconductors, I have computed the band splitting across 32×32×32 **k** points evenly

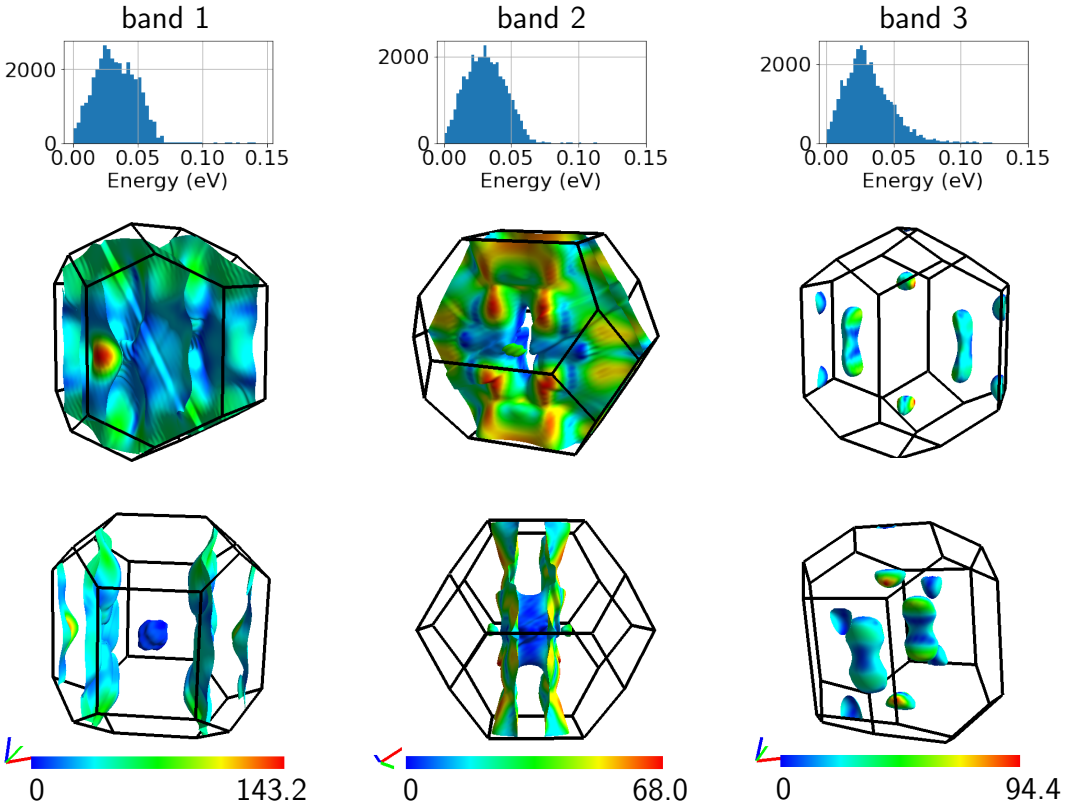

Figure 2.3: Band splitting plots and histograms for TaRuSi. The band splitting in meV due to spin-orbit coupling is plotted for **k** points on each branch of the Fermi surface for the system without spin-orbit coupling indicated by colour mapping. The top row are histograms of the band splitting across the Brillouin zone for bands corresponding with Fermi surfaces plotted underneath.

spaced throughout the first Brillouin zone for each band that crosses the Fermi energy. The results of this calculation are presented in Fig. 2.3 for TaRuSi and Fig. 2.4 for TaReSi. I have found that the band splitting is less than about 70 meV for all of the **k** points comprising the main branches of the Fermi surface of TaRuSi, while there are a few small pockets of the Fermi surface containing **k** points at which the band splitting is over 100 meV. In contrast, the main branches of the Fermi surface of TaReSi each contain many **k** points at which the band splitting is over 100 meV. The average band splitting is calculated by considering **k** points at which one of the split bands is above the Fermi energy and the other below. I refer to the average taken in this way as E_{ASOC}. E_{ASOC} computed in this way provides and estimate of the average band splitting across points on the Fermi surface. I have found $E_{\mathrm{ASOC}} = 41$ meV for TaRuSi and $E_{\mathrm{ASOC}} = 81$ meV for TaReSi. The band splitting of TaRuSi is comparable to that of $LaNiC_2$ [15],

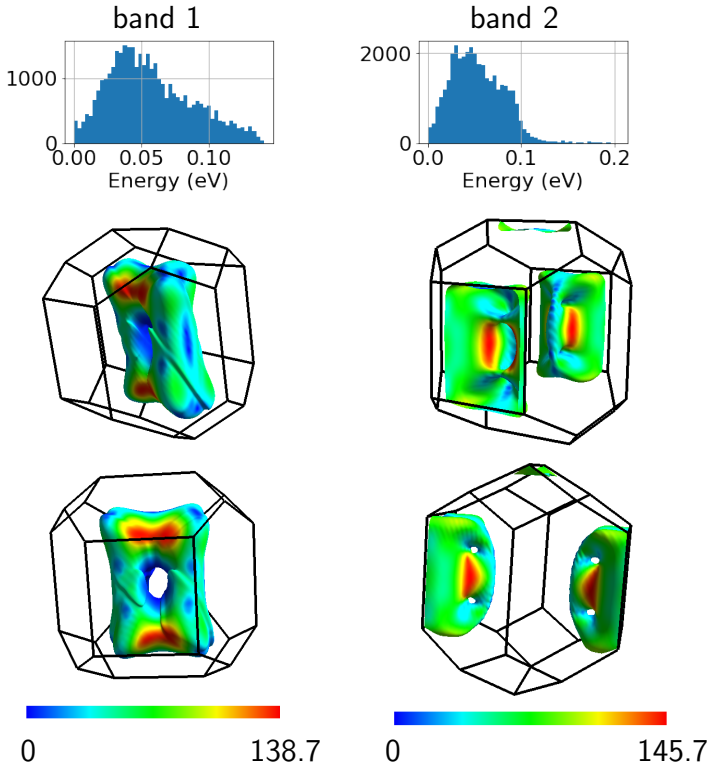

Figure 2.4: Band splitting plots and histograms for TaReSi. The band splitting in meV due to spin-orbit coupling is plotted for **k** points on each branch of the Fermi surface for the system without spin-orbit coupling indicated by colour mapping. The top row are histograms of the band splitting across the Brillouin zone for bands corresponding with Fermi surfaces plotted underneath.

which is also thought to have weak spin-orbit coupling allowing for a non-unitary triplet pairing state [18]. The band splitting of TaReSi is comparable to that of $CePt_3Si$ [36] which is thought to have significant SOC [36].

2.3 Discussion

Symmetry analysis of the superconducting gap function for materials with the C_{2v} point group dictates that time-reversal symmetry breaking is only possible in the limit of weak spin-orbit coupling. In this limit, the only states that break time-reversal symmetry are the non-unitary triplet states. This argument was given to predict the nature of the superconducting state of $LaNiC_2$ for which muon spin relaxation experiments have shown evidence of time-reversal symmetry

breaking [18]. Spin-orbit coupling is assumed to be sufficiently weak in $LaNiC_2$ as to allow for a time-reversal-symmetry-broken superconducting state. Density functional theory calculations for $LaNiC_2$ have estimated the spin-orbit coupling energy scale to be E_{ASOC} =42 meV so that $E_{\mathrm{ASOC}}/k_BT_c \approx 181$.

Given the point group of TaRuSi and TaReSi is C_{2v}, the symmetry analysis applied to the superconducing state of $LaNiC_2$ is directly applicable to TaRuSi and TaReSi. Recent muon spin relaxation experiments have shown evidence that time-reversal symmetry is broken in the superconducting state of TaRuSi and preserved in the superconducting state of TaReSi. We can therefore use symmetry arguments to conclude that the superconducting state of TaRuSi should be a non-unitary triplet state. The only conclusion that can be made for TaReSi given time-reversal preservation is that the superconducting state is not a non-unitary triplet state. The superconducting state of TaReSi may be a singlet, unitary triplet, or mixed singlet-triplet state.

I have shown by density functional theory calculations that the DFT band structure and Fermi surfaces are weakly affected by the inclusion of spin-orbit coupling in TaRuSi, while the DFT band structure and Fermi surfaces are significantly modified by the inclusion of spin-orbit coupling in TaReSi. The spin-orbit coupling energy scale was estimated to be E_{ASOC} =41 meV for TaRuSi so that $E_{\mathrm{ASOC}}/k_BT_c \approx 138$ and E_{ASOC} =81 meV for TaReSi so that $E_{\mathrm{ASOC}}/k_BT_c \approx 192$, which are each close to the value estimated for $LaNiC_2$. While the average value of E_{ASOC} =81 meV is not particularly large for TaReSi, the main branches of the Fermi surface contain **k**-points at which the band splitting is around 150 meV, while the band splitting is only significantly above 70 meV for a few small pockets of the Fermi surface for TaRuSi.

Chapter 3

Tunable Dirac Surface states in Disordered Intermetallic Superconductor $BiPd_{1-x}Pt_x$

3.1 Background and Experimental Observations

In principle, topologically non-trivial surface states in proximity to bulk superconductivity can realize non-abelian Majorana bound states [11]. The existence of Majorana states within the superconducting state is a characteristic feature of topological superconductivity, and is the most important for practical applications. That is, a topological superconductor could be used to form stable qubits in quantum-information devices through braiding of the Majorana bound states. A nice review of the relationship between Majorana states and topological superconductivity is given in Ref.[39]. It was shown that a topological superconductor can be realized in theory by creating a heterostructure with a topological insulator (TI) such as Bi_2Se_3 and an s-wave superconductor such that superconductivity is induced in the topological surface states of the TI through the proximity effect [11]. Similarly, it was argued that topologically non-trivial band structure and Dirac surface states of the intrinsic superconductor $FeSe_{0.5}Te_{0.5}$ calculated by DFT should allow for topological superconductivity in the surface states through proximity to bulk superconductivity [48].

Bi- and Pd-based compounds have attracted attention recently as possible realizations of topological superconductivity. Recently, a Dirac cone dispersion was imaged in ARPES measurements of α-BiPd within 0.6 eV of the Fermi energy [5]. Similar linearly dispersing spectra were seen in α-Bi_2Pd [9] and β-Bi_2Pd [35]. The results of pressure-dependent μ-SR experiments on β-Bi_2Pd [35] indicate an un-

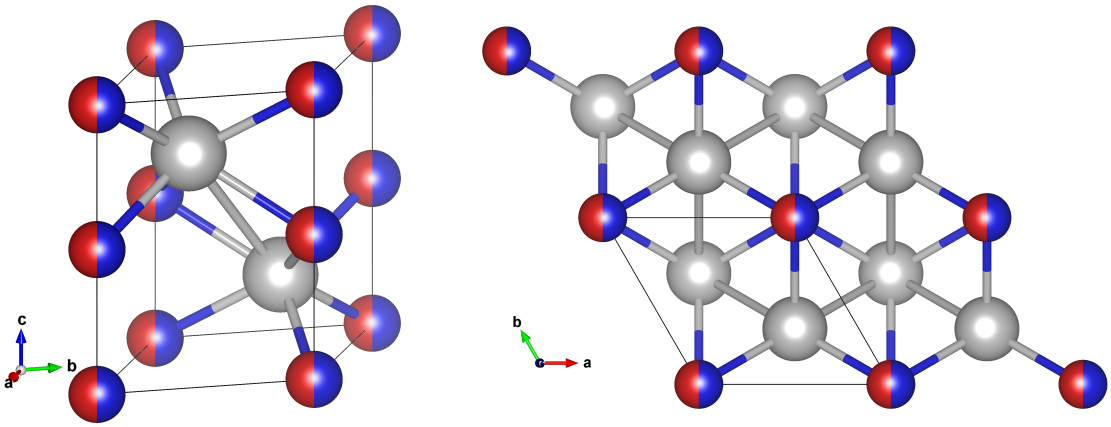

Figure 3.1: Crystal structure of Bi_2PdPt. Grey sites represent Bi atoms and half red/blue sites represent a uniform random distribution of Pd and Pt atoms.

Compound	SR-LDA	FR-LDA	SR-GGA	FR-GGA	XRD
γ-BiPd	3.86, 5.17	4.22, 5.57	4.31, 5.75	4.34, 5.77	4.23, 5.69 [4]
Bi_2PdPt	3.87, 5.11	4.22, 5.44	4.42, 5.67	4.42, 5.64	4.29, 5.57 [20]
BiPt	3.90, 5.21	4.32, 5.47	4.42, 5.57	4.44, 5.58	4.32, 5.49 [53]

Table 3.1: Lattice constants a/b, c (Å) as obtained from DFT relaxation calculations and XRD experiments at room temperature. All values are rounded to the third digit.

conventional linear dependence between the superconducting critical temperature and the superfluid density analagous to the cuprate unconventional superconductors [8]. It is also claimed by the authors of Ref.[8] that the strong pressure dependence of the superfluid density is incompatible with an electron-phonon mediated pairing process. The results of these experiments provide strong motivation for investigating the electronic structure of related compounds.

Bi_2PdPt forms a hexagonal crystal structure as shown in Fig. 3.1. Lattice constants determined by x-ray diffraction experiments (XRD) and DFT calculations are given in Table 3.1. Anti-site disorder is present at the Pd/Pt sites such that the Pd and Pt atoms occupy equivalent sites, each with 50% probability. It is a special case of the series $BiPd_{1-x}Pt_x$ with $x = 0.5$. The limiting cases are the parent compounds, BiPt when $x = 1$ and γ-BiPd when $x = 0$. While BiPd has been synthesized in the high-temperature γ phase [4], it is presumably less stable than the lower temperature α and β phases. However, nanoparticles of BiPd in the γ phase have been cooled to low temperatures without structural phase transition, and a superconducting transition temperature of 3.2 K was measured [16].

Measured lattice constants for nanocrystalline γ-BiPd are close to the XRD measurement values given in Table 3.1. The authors of Ref.[16] have also reported that annealing γ-BiPd nanocrystals at 673 K produced a structural transition to the β phase indicating metastability of the γ phase. I will show in the next section that γ-BiPd is predicted to be stable for bulk crystals as well on the basis of phonon calculations.

γ-BiPd and BiPt are isoelectronic and have nearly identical lattice structure, while Pt has an atomic number, Z, which is about 1.7 times that of Pd. Therefore, the substitution fraction, x, in the series $BiPd_{1-x}Pt_x$ can in theory be tuned to simultaneously control the effects of spin-orbit coupling and electron-phonon coupling. This is because spin-orbit coupling is estimated to scale as Z^2 [24], which is followed approximately when comparing 4d and 5d elements in the same group such as Pd and Pt [41], and the large mass difference between Pd and Pt is expected to significantly alter the phonon frequencies. In some disordered materials, it is reasonable to believe that tuning the amount of disorder could produce topological phase transitions, or allow for manipulation of the binding energy of topological surface states. For example, it is predicted that Dirac cones in iron chalcogenides can be tuned closer to the Fermi energy through atomic substitution, with the compound $FeSe_{0.325}I_{0.175}Te_{0.5}$ in particular predicted to realize a Dirac-cone surface state very close to the Fermi energy from the results of a coherent-potential approximation calculation [25].

While it is unclear whether the γ phase of a bulk crystal of BiPd may be stabilized at low enough temperatures to measure a possible superconducting transition, it is clear that $BiPd_{1-x}Pt_x$ with $x = 0.5$ is stable below a superconducting critical temperature [20]. The substitution fraction, x, may then possibly be tuned below 0.5. In the next section, I will show that a Dirac-cone topological surface state near the Fermi energy is predicted from DFT calculations for the series $BiPd_{1-x}Pt_x$. The Dirac cone is found to have a binding energy of about 0.5 eV below the Fermi energy in the limit $x = 1$, and binding energy within 0.1 eV of the Fermi energy in the limit $x = 0$.

3.2 Electronic Structure

Fully-relativistic and scalar-relativistic DFT calculations for the parent compounds, BiPt and γ-BiPd, were performed using Quantum Espresso [13]. A 12×12×12 Monkhorst-Pack **k**-point grid was used to sample the Brillouin zone for each system. Ultrasoft pseudopotentials with non-linear core correction as provided in the PSlibrary associated with Quantum Espresso were used. Kinetic energy cutoffs of 80 Ry for the wavefunctions and 640 Ry for the charge density were used. Cold

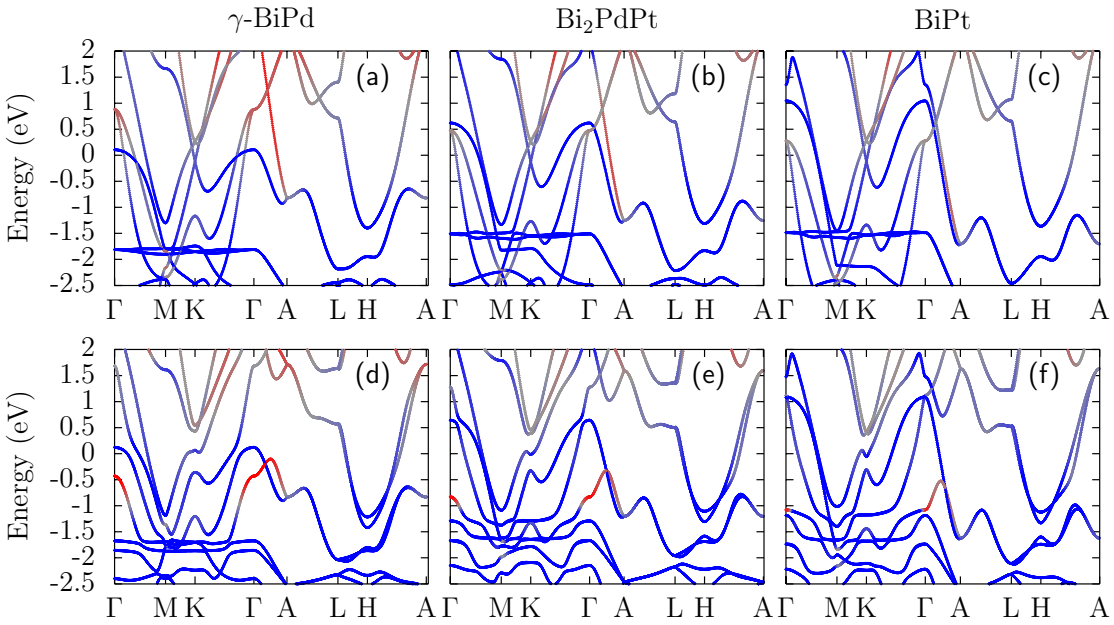

Figure 3.2: Band character plots for γ-BiPd, Bi_2PdPt, and BiPt. The band character is coloured by the projection onto Wannier orbitals centered on Bi atoms (red) and Pt/Pd atoms (blue). Bands plotted in (a-c) are calculated without the inclusion of SOC and bands plotted in (d-f) are calculated with SOC.

smearing [28] with degauss parameter of 0.01 Ry was used. Lattice constants are obtained by relaxing the system starting from the experimentally-determined structure until pressures on the unit cell are less than 0.05 kbar. A virtual-crystal pseudopotential for $Pd_{0.5}Pt_{0.5}$ was generated using the virtual_v2.x program associated with Quantum Espresso.

Maximally-localized Wannier functions were calculated using Wannier90 [31]. The initial projections for the Wannier functions were constructed using the Bi-s, Bi-p, Pd/Pt-s, Pd/Pt-p, Pd/Pt-d. The atom-projected density of states obtained from the projwfc.x program associated with Quantum Espresso was used to construct disentanglement windows in the Wannier function calculation. A wide disentanglement window of [-15, 21] eV was used, and a frozen window was chosen to contain the majority of the Bi-p and Pd/Pt-d, which is approximately [-6, 5] eV for each system. The obtained Wannier functions were then used to calculate orbital-projected band structures shown in Fig. 3.2. It can be seen in Fig. 3.2 that the Bi and Pd/Pt conduction orbitals are strongly hybridized, as expected for intermetallic compounds. Band inversion produced by the inclusion of SOC is found in each compound for the two bands within the energy range [0, 1.5] eV at

the Γ-point, which is reflected in the change of orbital character in Fig. 3.2. The effect is small in BiPt, while it is much more pronounced in γ-BiPd. It is also important to notice that there is a continuous direct gap separating one of the conduction bands (band #15) from the lower energy bands in each system. The Z_2 topological invariant is therefore well defined for the highest 14 valence bands.

Since $BiPd_{1-x}Pt_x$ is centrosymmetric, The Z_2 invariant may be calculated from parity product analysis. The non-symmorphic crystal symmetry enforces four-fold degeneracy of states with half even and half odd parity at the A and L points ensuring $\delta_A\delta_L^3 = 1$. The strong topological index is therefore equal to $\nu_0 = \delta_\Gamma\delta_M^3$, and the weak topological indices are each zero. The parity eigenvalues for the highest 14 (28 when counting Kramers degeneracy) valence bands at TRIM are given in Table 3.2. The Z_2 index is found to be non-trivial for γ-BiPd, and trivial for Bi_2PdPt and BiPt.

Surface state spectral functions were calculated using the iterative method defined in Ref.[37] for a semi-infinite system as implemented in the WannierTools library [49]. The bulk projected states and surface states for a (001) Pd/Pt-

γ-BiPd ($Z_2 = (1;0,0,0)$)															
	1	2	3	4	5	6	7	8	9	10	11	12	13	14	δ_i
Γ	+	−	+	+	+	+	+	+	+	+	+	+	−	+	+
M	−	+	+	+	+	+	−	+	+	+	+	−	+	+	−
L	(+	−)	(+	−)	(+	−)	(+	−)	(+	−)	(+	−)	(+	−)	−
A	(+	−)	(+	−)	(+	−)	(+	−)	(+	−)	(+	−)	(+	−)	−

Bi_2PdPt ($Z_2 = (0;0,0,0)$)															
	1	2	3	4	5	6	7	8	9	10	11	12	13	14	δ_i
Γ	+	−	+	+	+	+	+	+	+	+	+	+	−	+	+
M	−	+	+	+	+	+	−	+	+	+	−	+	−	+	+
L	(+	−)	(+	−)	(+	−)	(+	−)	(+	−)	(+	−)	(+	−)	−
A	(+	−)	(+	−)	(+	−)	(+	−)	(+	−)	(+	−)	(+	−)	−

BiPt ($Z_2 = (0;0,0,0)$)															
	1	2	3	4	5	6	7	8	9	10	11	12	13	14	δ_i
Γ	+	−	+	+	+	+	+	+	+	+	+	+	−	+	+
M	−	+	+	+	+	+	+	−	+	+	−	+	−	+	+
L	(+	−)	(+	−)	(+	−)	(+	−)	(+	−)	(+	−)	(+	−)	−
A	(+	−)	(+	−)	(+	−)	(+	−)	(+	−)	(+	−)	(+	−)	−

Table 3.2: Parities and parity products of the highest 14 valence bands for γ-BiPd, Bi_2PdPt, and BiPt.

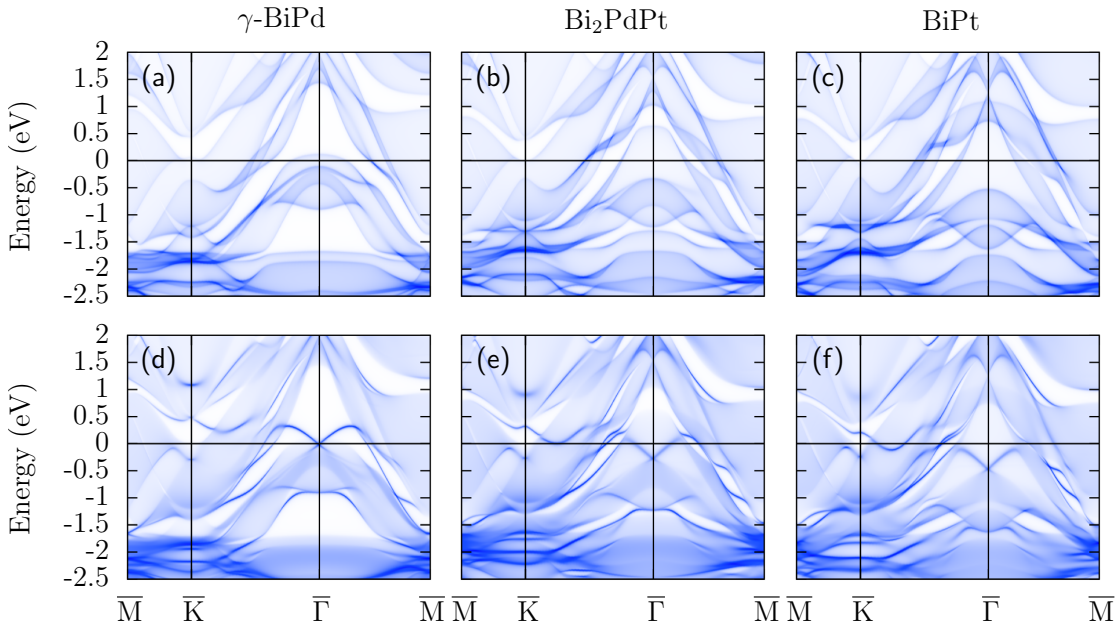

Figure 3.3: (a-c) Bulk projected states and (d-f) surface-state spectral functions of the (001) Pd/Pt-terminated surface for γ-BiPd, Bi_2PdPt, and BiPt.

terminated surface are plotted in Fig. 3.3. A Dirac cone in can be seen in the surface states with binding energy of at most about 0.5 eV. The Dirac cone binding energy is higher for BiPt and is very small for γ-BiPd.

Force constants used in phonon and electron-phonon calculations were calculated using density-functional perturbation theory as implemented in Quantum Espresso. Projector augmented-wave pseudopotentials, energy cutoffs of 45 Ry for the wavefunctions and 180 Ry for the charge density, and 8×8×8 **k** points were used in the the DFT calculation. 4×4×4 **q** points were used in the phonon calculation. The Eliashberg spectral functions and electron-phonon coupling were calculated using the EPW code with 4×4×4 **k** points used in the Wannier function calculation. Interpolation grids of 16×16×16 **k** points and 16×16×16 **q** points were used in the electron-phonon calculations.

The resulting phonon bands, phonon density of states, and Eliashberg spectral functions for γ-BiPd and BiPt are plotted in Fig. 3.4. It can be seen in the phonon spectrum of γ-BiPd that there are higher frequency phonon excitations in comparison with BiPt, which can be attributed to the lower mass of the Pd atom. I have found that the electron-phonon coupling, of about $\lambda = 0.8$ for γ-BiPd, is significantly larger than the value of about $\lambda = 0.45$ for BiPt. Given γ-BiPd has not been stabilized at low enough temperatures in order to study

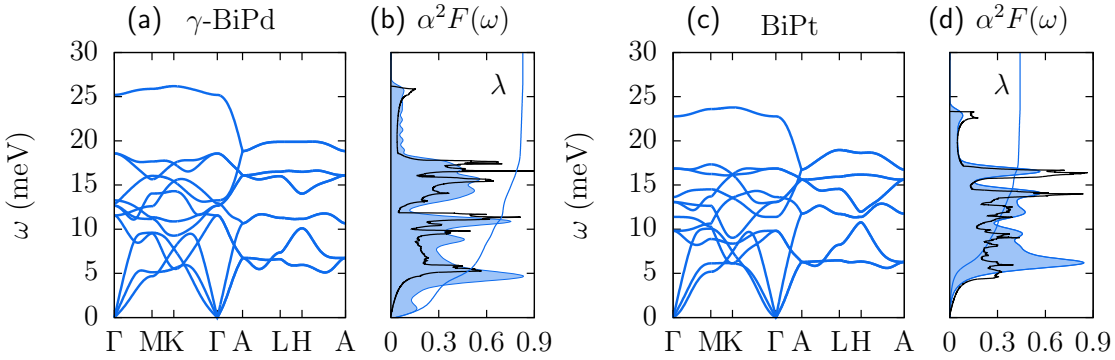

Figure 3.4: Phonon bands, phonon density of states (black), and Eliashberg spectral functions (blue) for γ-BiPd (a-b) and BiPt (c-d). The phonon density of states and Eliashberg spectral functions are scaled by a factor of 3 for better visualization. The solid blue line is the cumulative electron-phonon coupling.

the superconducting state to the best of my knowledge, it is worth mentioning that phonon calculations seem to imply that the structure is stable. Typically, a structural instability may be indicated in a phonon calculation by the presence of imaginary phonon frequencies for the unstable mode. This is not the case for γ-BiPd.

3.3 Discussion

In this chapter, I have shown that density functional theory predicts Dirac-cone surface states near the Fermi energy for x =0, 0.5, and 1 of the series $BiPd_{1-x}Pt_x$. The Z_2 topological invariant is calculated to be (0;0,0,0) for $x = 0.5$ and 1, and (1;0,0,0) for $x = 0$, which corresponds with the γ phase of BiPd. The binding energies of the Dirac cones are less than what has been experimentally observed recently for other Bi- and Pd-based systems, with the binding energy changing from about 0.5 eV to less than 0.1 eV as x is tuned from 1 to 0. The topological surface states in γ-BiPd could host Majorana states which may be useful in the implementation of a topological qubit. The non-trivial band topology could also produce unconventional properties of the superconducting state, such as the unconventional pressure dependence of T_c which was observed in α-Bi_2Pd [8].

While a bulk crystal of the high-temperature γ phase of BiPd has not been stabilized at low temperatures to the best of my knowledge, I have shown through DFT-based phonon calculations that the structure is expected to be at least metastable. Additionally, experiments have shown that nanocrystals of γ-BiPd

can be stabilized at low temperatures, and a superconducting critical temperature of 3.2 K was measured [16]. My DFT-based calculations provide some indication that bulk crystals of γ-BiPd may be able to realize topological superconductivity.

Chapter 4

Correlated Electronic Structure of Flat-Band Kagome Metal YCr_6Ge_6

4.1 Background and Experimental Observations

The Kagome lattice is a two-dimensional lattice of corner sharing triangles. Arguments based on tight-binding theory suggest that metallic materials with Kagome lattice structure may realize interesting band structure features such as a dispersionless flat band and Dirac points defined by a linear dispersion. The argument is as follows. Considering only nearest neighbour hopping, the tight-binding Hamiltonian is diagonalized by Fourier transform giving the bands, $\epsilon_1(\mathbf{k})$, $\epsilon_2(\mathbf{k})$, and $\epsilon_3(\mathbf{k})$. One of the bands, $\epsilon_1(\mathbf{k})$, has no dependence on $\mathbf{k}$ and is therefore completely flat throughout the Brillouin zone. The other two bands, $\epsilon_2(\mathbf{k})$ and $\epsilon_3(\mathbf{k})$, cross at only a single point in the Brillouin zone (the K point) forming a linearly dispersing cone. This is referred to as a Dirac cone due to the similarity between the tight-binding Hamiltonian around this point and the Dirac equation for massless particles.

Of course, electrons in a real material are not limited to a tight-binding description with only nearest-neighbour hopping, and therefore the expected flat band will have a finite width. Spin-orbit coupling is expected to open a band gap at the Dirac point. DFT allows us to construct a more realistic model describing these systems, and we may study the effect of electronic correlations with DFT+DMFT.

Recently discovered Kagome metals include the 11-type systems such as CoSn and FeSn, the 135-type systems such as CsV_3Sb_5, and the 166-type systems such as YCr_6Ge_6. Unlike the 11 and 135 Kagome metals, which form a single-layered

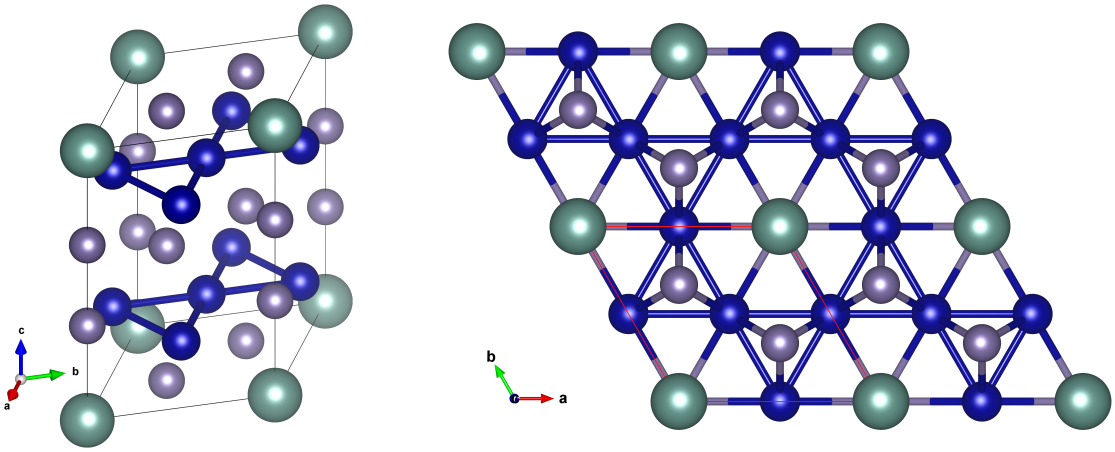

Figure 4.1: Lattice structure of YCr_6Ge_6. Y, Cr, and Ge atoms are represented by green, grey, and blue sites respectively. The unit cell of YCr_6Ge_6 is depicted in the left and the 2×2×1 cell as viewed from the c-axis is depicted on the right.

Kagome lattice, the unit cell for the 166 materials contains two Kagome lattices. One consequence of this geometry is that some ligands surrounding the transition metal atom are typically not centered on sites of high symmetry. While the transition metals experience a hexagonal crystal field in the 11 and 135 Kagome metals, this is not necessarily the case for the 166 systems.

The focus of this chapter will be on the 166 Kagome system, YCr_6Ge_6. The lattice structure of YCr_6Ge_6 is shown in Fig. 4.1. Previous DFT calculations for this material have revealed that the calculated band structure contains a very flat band close to the Fermi energy [52]. Recent measurements of the spectral function from angle-resolved photoemission spectroscopy (ARPES) also provides evidence for the presence of this flat band [50]. When comparing the measured band structure with DFT band structure, the band renormalization factor, which may be defined as in e.g. Eq. 1.33, is estimated to be $Z^{-1} \sim 1.6$ [50]. This indicates that important correlation effects are neglected in the DFT calculations, and that the electronic structure should be more accurately described by the results of a DFT+DMFT calculation.

In general, correlation effects should not be neglected for flat band systems since even for relatively small values of the Coulomb repulsion, U, the ratio U/t is extremely large with t close to the ideal limit $t = 0$.

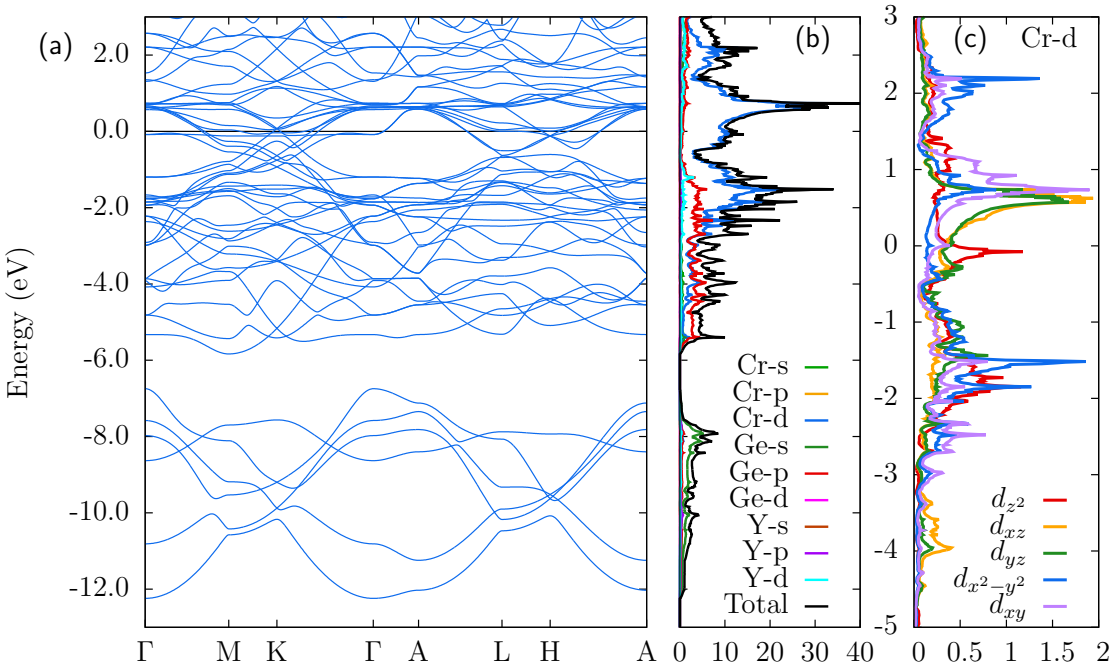

Figure 4.2: (a) DFT band structure for YCr_6Ge_6, (b) total and orbital-projected density of states, and (c) projected density of states for a Cr atom.

4.2 Electronic Structure

The DFT calculation is performed using Quantum Espresso [13]. The Brillouin zone is sampled over a 6×6×6 Monkhorst-Pack grid to solve the DFT self-consistency condition while the density of states were calculated over a dense 24×24×24 grid. Smearing is included within the m-p scheme [30] with a degauss parameter of 0.01 Ry. Projector augmented wave pseudopotentials with non-linear core correction as provided in the PSlibrary associated with Quantum Espresso were used. The resulting band structure and density of states are plotted in Fig. 4.2.

A flat band within the (h,k,0) plane about 0.1 eV below to the Fermi energy can be seen in the DFT band structure. Flat dispersion is also formed by many bands within the energy window [0.5,0.75] eV causing a large peak in the density of states. Dirac points can be seen at the K points about 0.1 eV above the Fermi energy, which is similar to the Dirac points seen in $TbMn_6Sn_6$ [51], as well as the multiple other Mn-based 166-type Kagome systems studied in Ref.[26]. In the case of $TbMn_6Sn_6$, SOC has the effect of opening a Chern gap at the Dirac point [51].

Maximally-localized Wannier functions were obtained using Wannier90 [31]. Due to the absence of continuous band gaps in the DFT band structure, it is

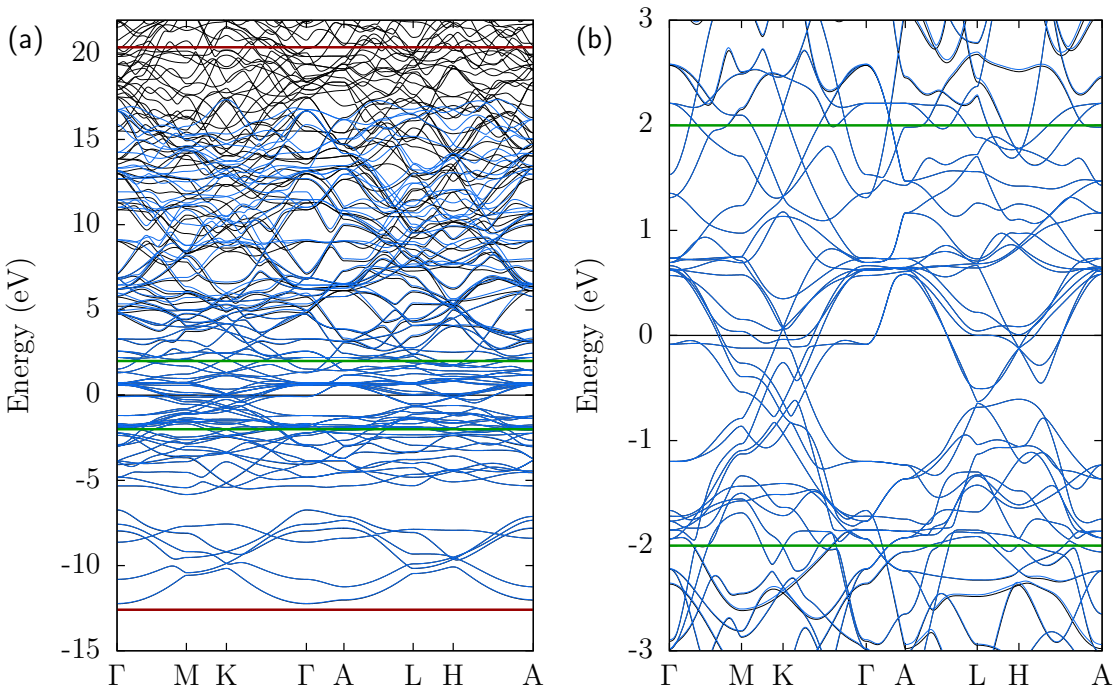

Figure 4.3: Wannier bands (blue) obtained from the disentanglement procedure and DFT bands (black). Red and green lines indicate the disentanglement window and frozen window respectively. (a) and (b) contain the same data plotted on different energy scales.

necessary to include disentanglement in the wannierization. The initial projectors used were Y-p, Y-d, Cr-s, Cr-p, Cr-d, Ge-s, Ge-p. The resulting Wannier bands overlayed with the DFT bands and disentanglement windows used can be seen in Fig. 4.3 The Wannier bands are in excellent agreement with the DFT bands near the Fermi energy. The Wannier-orbital character of the bands is plotted in Fig. 4.4. It can be seen in Fig. 4.4 that the flat band below the Fermi energy is mainly of d_{z^2} character while the Dirac cone at the K point is mainly of $d_{x^2-y^2}/d_{xy}$ character.

Wannier-orbital projection of the band structure indicates that the flat band near the Fermi energy is primarily of d_{z^2} character, while the Dirac cone is primarily of $d_{xy}/d_{x^2-y^2}$ character.

DFT+DMFT calculations were performed to study the influence of additional electron-electron interactions. A density-density interaction Hamiltonian is used with Kanamori U and U' matrices constructed using $\bar{U} = 4$ eV and $J_H = 0.7$ eV. The double counting correction defined in Ref.[17] was used. The continuous-

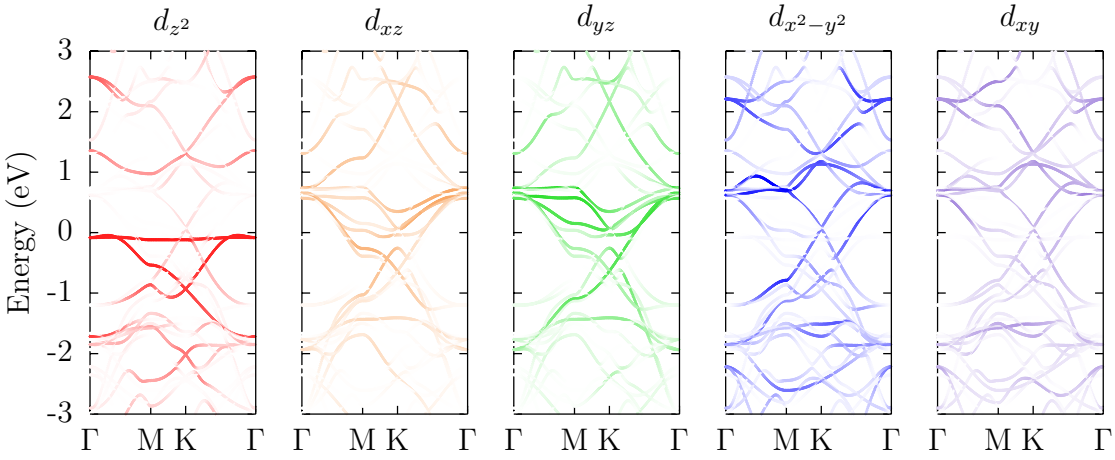

Figure 4.4: Wannier-orbital character of DFT bands.

time hybridization-expansion quantum Monte Carlo method, as implemented in the TRIQS/CTHYB [40] library, was used to calculate the impurity Green's function in each iteration of the DMFT cycle. 512×10^7 Monte Carlo samples were used, with a sample taken every 200 Monte Carlo steps. The correlated subspace consists of all 10 Cr-d orbitals. 13 iterations of the DMFT cycle were completed with paramagnetism enforced. The inverse temperature was set to $\beta = 40$ eV^{-1} corresponding with a temperature of around $T = 290$ K. The DFT calculation was performed using WIEN2k with the LDA exchange-correlation functional. Wannier projectors were constructed using the method described in Ref.[3] as implemented in the dmftproj program associated with the TRIQS/DFTTools library [1]. A wide energy window of [-13, 10] eV was used in the construction of the Wannier projectors.

The resulting DFT+DMFT impurity self energies and spectral function are plotted in Fig. 4.5. It can be seen in Fig. 4.5 that strong electron-electron correlations have the effect of renormalizing the flat bands even closer to the Fermi energy, resulting in a continuous flat band across the plotted Brillouin zone path. The spectrum is fairly incoherent in the energy window plotted aside from the lower, primarily uncorrelated, Ge-p bands, and near the Fermi energy where $\mathrm{Im}\Sigma(\omega)$ is close to zero. A similar effect was observed in the DFT+DMFT spectral function of LaFeAsO [2].

The orbital occupation and mass enhancement factors obtained in the DFT+DMFT calculation are given in Table 4.2. The average occupation of the d orbitals is 0.871 which is close to half filling. I have found that the d_{z^2} orbitals have a larger mass enhancement which could be due to strong correlations originating from the

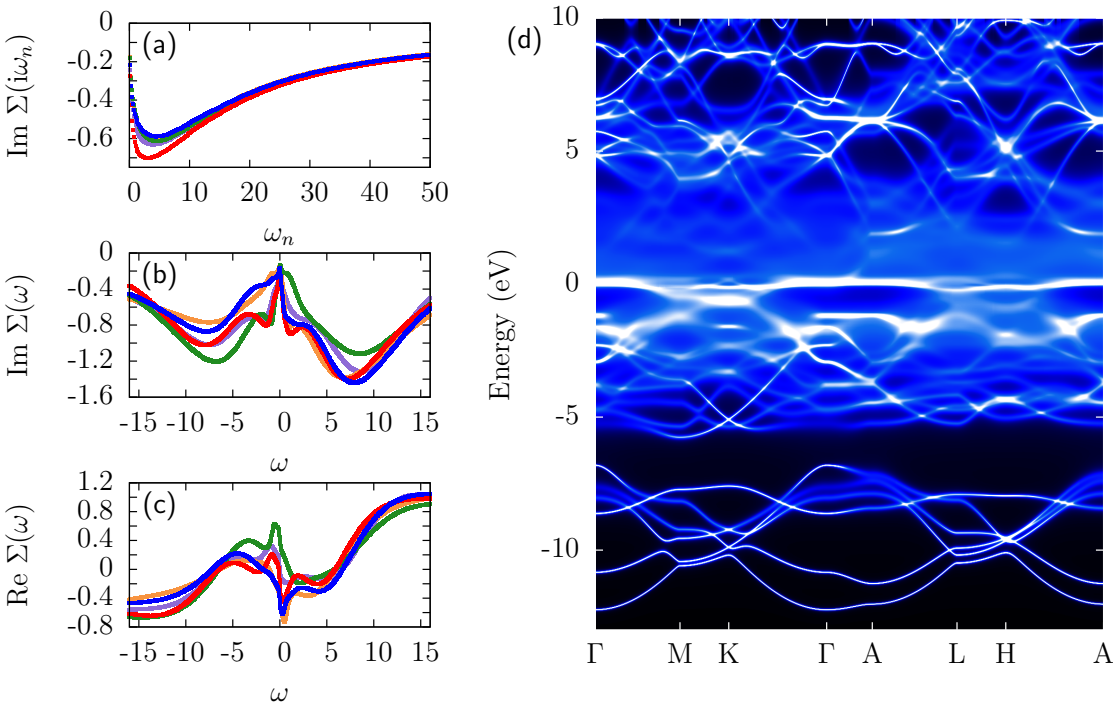

Figure 4.5: (a) Imaginary part of the impurity self energy as a function of Matsubara frequency, (b) imaginary part and (c) real part of the analytically continued impurity self energy as a function of real frequency, and (d) spectral function for YCr_6Ge_6 obtained from DFT+DMFT.

flat band. The other four orbitals have a significant mass enhancement within 1.6-1.7, and the average mass enhancement factor is found to be 1.733. This is in fairly close agreement with the value of 1.6 estimated by fitting scaled DFT bands to ARPES measurements [50].

4.3 Discussion

The characteristic flat band feature of Kagome-lattice systems was found to be surprisingly close to the Fermi energy for YCr_6Ge_6 from previous DFT-based studies [52]. More recent ARPES measurements have confirmed the appearance of flat band near the Fermi energy [50]. A typical sign of strong electron-electron correlations in a material is the strong renormalization of DFT bands when compared with ARPES spectra causing apparent mass enhancement of the conduction electrons. A renormalization factor of around 1.6 was found in this way by the authors

	d_{z^2}	d_{xz}	d_{yz}	$d_{x^2-y^2}$	d_{xy}	ave.
occ.	0.873	0.920	0.762	1.022	0.777	0.871
m^*/m^{DFT}	1.954	1.659	1.697	1.676	1.677	1.733

Table 4.1: Orbital occupation and mass enhancement from DFT+DMFT.

of Ref.[50]. Significant electron-electron correlation effects are therefore clearly neglected in previous DFT works given the estimated renormalization. Additionally, electron-electron interactions are expected to be amplified between states forming a flat band due to the large U/t ratio.

In this chapter, I have examined the effects of strong electron-electron interactions on the electronic structure of the flat-band Kagome metal YCr_6Ge_6, which are neglected in DFT calculations. I have obtained the lattice spectral function from the results of DFT+DMFT calculations. I have found that a large amount of spectral weight is renormalized towards the Fermi energy forming a coherent flat bands across much of the Brillouin zone, spanning a much wider range of the Brillouin zone than what is seen in DFT calculations. The average renormalization factor of $Z^{-1} = 1.733$ obtained from my DFT+DMFT calculations is in agreement with the value estimated by comparing DFT bands to ARPES spectra [50].

Chapter 5

Concluding Remarks

I have presented standard methods for calculating and analyzing the electronic structure of material systems starting from first principles. The key component of each method is density functional theory, which provides a means of calculating the charge density and a useful basis of single-particle wavefunctions. I have shown that the results of a DFT calculation can be used to provide insight into complex properties of materials. For example, the nature of superconductivity, effects arising from non-trivial band-structure topology, and strong electron-electron correlations.

In Chapter 2, I have argued that the superconducting state of the non-centrosymmetric superconductor, TaRuSi, should be a non-unitary triplet-pairing state. This follows from symmetry analysis, and is consistent with my DFT-based estimation of the strength of spin-orbit coupling. In Chapter 3, I have characterized the band topology of a set of superconductors, γ-BiPd, Bi_2PdPt, and BiPt, showing non-trivial topological properties and Dirac surface states which can be tuned close to the Fermi energy. The electron-phonon coupling was calculated and is found to be much higher in γ-BiPd than in BiPt. While the γ structural phase is the high-temperature phase of BiPd, I have shown that phonon calculations suggest that the structure may be metastable at low temperatures. In Chapter 4, I have studied the effects of strong electron-electron interactions on the spectral function of the flat-band Kagome metal, YCr_6Ge_6. My results reveal that much of the spectral weight near the Fermi energy is renormalized, forming a coherent flat band very close to the Fermi energy.

References

[1] M. Aichhorn, L. Pourovskii, P. Seth, V. Vildosola, M. Zingl, O. E. Peil, X. Deng, J. Mravlje, G. J. Kraberger, C. Martins, M. Ferrero, and O. Parcollet. Triqs/dfttools: A triqs application for ab initio calculations of correlated materials. *Computer Physics Communications*, 204:200–208, 2016. doi:10.1016/j.cpc.2016.03.014.

[2] M. Aichhorn, V. Pourovskii, L.and Vildosola, M. Ferrero, O. Parcollet, T. Miyake, A. Georges, and S. Biermann. Dynamical mean-field theory within an augmented plane-wave framework: Assessing electronic correlations in the iron pnictide LaFeAsO. *Phys. Rev. B*, 80:085101, 2009. doi:10.1103/PhysRevB.80.085101.

[3] V. I. Anisimov, D. E. Kondakov, A. V. Kozhevnikov, I. A. Nekrasov, Z. V. Pchelkina, J. W. Allen, S.-K. Mo, H.-D. Kim, P. Metcalf, S. Suga, A. Sekiyama, G. Keller, I. Leonov, X. Ren, and D. Vollhardt. Full orbital calculation scheme for materials with strongly correlated electrons. *Phys. Rev. B*, 71:125119, 2005. doi:10.1103/PhysRevB.71.125119.

[4] P. Bayliss. Revised unit-cell dimensions, space group, and chemical formula of some metallic minerals. *The Canadian Mineralogist*, 28(4):751–755, 1990.

[5] H. M. Benia, E. Rampi, C. Trainer, C. M. Yim, A. Maldonado, D. C. Peets, A. Stöhr, U. Starke, K. Kern, A. Yaresko, G. Levy, A. Damascelli, C. R. Ast, A. P. Schnyder, and P. Wahl. Observation of dirac surface states in the noncentrosymmetric superconductor BiPd. *Phys. Rev. B*, 94:121407, 2016. doi:10.1103/PhysRevB.94.121407.

[6] C. Buzea and T. Yamashita. Review of the superconducting properties of MgB_2. *Superconductor Science and Technology*, 14(11):R115, 2001. doi:10.1088/0953-2048/14/11/201.

[7] D. M. Ceperley and B. J. Alder. Ground state of the electron gas by a stochastic method. *Phys. Rev. Lett.*, 45:566–569, 1980. doi:10.1103/PhysRevLett.45.566.

[8] D. Das, R. Gupta, C. Baines, H. Luetkens, D. Kaczorowski, Z. Guguchia, and R. Khasanov. Unconventional pressure dependence of the superfluid density in the nodeless topological superconductor $\alpha-PdBi_2$. *Phys. Rev. Lett.*, 127:217002, 2021. doi:10.1103/PhysRevLett.127.217002.

[9] K. Dimitri, M. M. Hosen, G. Dhakal, H. Choi, F. Kabir, C. Sims, D. Kaczorowski, T. Durakiewicz, J.-X. Zhu, and M. Neupane. Dirac state in a centrosymmetric superconductor $\alpha-PdBi_2$. *Phys. Rev. B*, 97:144514, 2018. doi:10.1103/PhysRevB.97.144514.

[10] S. L. Dudarev, G. A. Botton, S. Y. Savrasov, C. J. Humphreys, and A. P. Sutton. Electron-energy-loss spectra and the structural stability of nickel oxide: An LSDA+U study. *Phys. Rev. B*, 57:1505–1509, 1998. doi:10.1103/PhysRevB.57.1505.

[11] L. Fu and C. L. Kane. Superconducting proximity effect and majorana fermions at the surface of a topological insulator. *Phys. Rev. Lett.*, 100:096407, 2008. doi:10.1103/PhysRevLett.100.096407.

[12] A. Georges, G. Kotliar, W. Krauth, and M. J. Rozenberg. Dynamical mean-field theory of strongly correlated fermion systems and the limit of infinite dimensions. *Rev. Mod. Phys.*, 68:13–125, 1996. doi:10.1103/RevModPhys.68.13.

[13] P. Giannozzi, S. Baroni, N. Bonini, M. Calandra, R. Car, C. Cavazzoni, D. Ceresoli, G. L. Chiarotti, M. Cococcioni, I. Dabo, A. Dal Corso, S. de Gironcoli, S. Fabris, G. Fratesi, R. Gebauer, U. Gerstmann, C. Gougoussis, A. Kokalj, M. Lazzeri, L. Martin-Samos, N. Marzari, F. Mauri, R. Mazzarello, S. Paolini, A. Pasquarello, L. Paulatto, C. Sbraccia, S. Scandolo, G. Sclauzero, A. P. Seitsonen, A. Smogunov, P. Umari, and R. M. Wentzcovitch. Quantum espresso: a modular and open-source software project for quantum simulations of materials. *Journal of Physics: Condensed Matter*, 21(39):395502, 2009. doi:10.1088/0953-8984/21/39/395502.

[14] F. Giustino, M. L. Cohen, and S. G. Louie. Electron-phonon interaction using wannier functions. *Phys. Rev. B*, 76:165108, 2007. doi:10.1103/PhysRevB.76.165108.

[15] I. Hase and T. Yanagisawa. Electronic structure of $RNiC_2$ (R=La, Y, and Th). *Journal of the Physical Society of Japan*, 78(8):084724–084724, 2009. doi:10.1143/jpsj.78.084724.

[16] Ma. Heise, J.-H. Chang, R. Schönemann, T. Herrmannsdörfer, J. Wosnitza, and M. Ruck. Full access to nanoscale bismuth–palladium intermetallics by

low-temperature syntheses. *Chemistry of Materials*, 26(19):5640–5646, 2014. doi:10.1021/cm502315a.

[17] K. Held. Electronic structure calculations using dynamical mean field theory. *Advances in Physics*, 56(6):829–926, 2007. doi:10.1080/00018730701619647.

[18] A. D. Hillier, J. Quintanilla, and R. Cywinski. Evidence for time-reversal symmetry breaking in the noncentrosymmetric superconductor lanic$_2$. *Phys. Rev. Lett.*, 102:117007, 2009. doi:10.1103/PhysRevLett.102.117007.

[19] J. Kanamori. Electron correlation and ferromagnetism of transition metals. *Progress of Theoretical Physics*, 30(3):275–289, 1963. doi:10.1143/PTP.30.275.

[20] A. Kataria, T. Agarwal, S. Sharma, D. Singh, S. Marik, and R. P. Singh. Superconductivity in Bi based Bi_2PdPt. *Mater. Adv.*, 3:5375–5382, 2022. doi:10.1039/D2MA00324D.

[21] D. D. Koelling and B. N. Harmon. A technique for relativistic spin-polarised calculations. *Journal of Physics C: Solid State Physics*, 10(16):3107, 1977. doi:10.1088/0022-3719/10/16/019.

[22] W. Kohn and L. J. Sham. Self-consistent equations including exchange and correlation effects. *Phys. Rev.*, 140:A1133–A1138, 1965. doi:10.1103/PhysRev.140.A1133.

[23] G. J. Kraberger, R. Triebl, M. Zingl, and M. Aichhorn. Maximum entropy formalism for the analytic continuation of matrix-valued green's functions. *Phys. Rev. B*, 96:155128, 2017. doi:10.1103/PhysRevB.96.155128.

[24] L. D. Landau and E. M. Lifshitz. Vol. 3. quantum mechanics–non-relativistic theory. *Course of Theoretical Physics, Pergamon Press, Oxford*, 1991.

[25] L. Lauke, R. Heid, M. Merz, T. Wolf, A.-A. Haghighirad, and J. Schmalian. Band engineering of dirac cones in iron chalcogenides. *Phys. Rev. B*, 102:054209, 2020. doi:10.1103/PhysRevB.102.054209.

[26] Y. Lee, R. Skomski, X. Wang, P. P. Orth, A. K. Pathak, B. N. Harmon, R. J. McQueeney, and L. Ke. Interplay between magnetism and band topology in kagome magnets RMn_6Sn_6. 2022. arXiv:2201.11265.

[27] A. H. MacDonald and S. H. Vosko. A relativistic density functional formalism. *Journal of Physics C: Solid State Physics*, 12(15):2977, 1979. doi:10.1088/0022-3719/12/15/007.

[28] N. Marzari, D. Vanderbilt, A. De Vita, and M. C. Payne. Thermal contraction and disordering of the Al(110) surface. *Phys. Rev. Lett.*, 82:3296–3299, 1999. doi:10.1103/PhysRevLett.82.3296.

[29] Nicola Marzari, Arash A. Mostofi, Jonathan R. Yates, Ivo Souza, and David Vanderbilt. Maximally localized wannier functions: Theory and applications. *Rev. Mod. Phys.*, 84:1419–1475, Oct 2012. URL: https://link.aps.org/doi/10.1103/RevModPhys.84.1419, doi:10.1103/RevModPhys.84.1419.

[30] M. Methfessel and A. T. Paxton. High-precision sampling for brillouin-zone integration in metals. *Phys. Rev. B*, 40:3616–3621, 1989. doi:10.1103/PhysRevB.40.3616.

[31] A. A. Mostofi, J. R. Yates, Y.-S. Lee, I. Souza, D. Vanderbilt, and N. Marzari. wannier90: A tool for obtaining maximally-localised wannier functions. *Computer physics communications*, 178(9):685–699, 2008. doi:10.1016/j.cpc.2007.11.016.

[32] Sajilesh K. P. and R. P. Singh. Superconducting properties of the noncentrosymmetric superconductors TaXSi (X = Re, Ru). *Superconductor Science and Technology*, 34(5):055003, 2021. doi:10.1088/1361-6668/abe4b7.

[33] J. P. Perdew, K. Burke, and M. Ernzerhof. Generalized gradient approximation made simple. *Phys. Rev. Lett.*, 77:3865–3868, 1996. doi:10.1103/PhysRevLett.77.3865.

[34] J. Quintanilla, A. D. Hillier, J. F. Annett, and R. Cywinski. Relativistic analysis of the pairing symmetry of the noncentrosymmetric superconductor $LaNiC_2$. *Phys. Rev. B*, 82:174511, 2010. doi:10.1103/PhysRevB.82.174511.

[35] M. Sakano, K. Okawa, M. Kanou, H. Sanjo, T. Okuda, T. Sasagawa, and K. Ishizaka. Topologically protected surface states in a centrosymmetric superconductor β-$PdBi_2$. *Nature Communications*, 6(1):8595, 2015. doi:10.1038/ncomms9595.

[36] K. V. Samokhin, E. S. Zijlstra, and S. K. Bose. $CePt_3Si$: An unconventional superconductor without inversion center. *Phys. Rev. B*, 69:094514, 2004. doi:10.1103/PhysRevB.69.094514.

[37] M. P. Lopez Sancho, J. M. Lopez Sancho, J. M. L. Sancho, and J. Rubio. Highly convergent schemes for the calculation of bulk and surface green functions. *Journal of Physics F: Metal Physics*, 15(4):851, 1985. doi:10.1088/0305-4608/15/4/009.

[38] A. Sanna, C. Pellegrini, and E. K. U. Gross. Combining eliashberg theory with density functional theory for the accurate prediction of superconducting transition temperatures and gap functions. *Phys. Rev. Lett.*, 125:057001, 2020. doi:10.1103/PhysRevLett.125.057001.

[39] M. Sato and S. Fujimoto. Majorana fermions and topology in superconductors. *Journal of the Physical Society of Japan*, 85(7):072001, 2016. doi:10.7566/JPSJ.85.072001.

[40] P. Seth, I. Krivenko, M. Ferrero, and O. Parcollet. Triqs/cthyb: A continuous-time quantum monte carlo hybridisation expansion solver for quantum impurity problems. *Computer Physics Communications*, 200:274–284, 2016. doi:10.1016/j.cpc.2015.10.023.

[41] K. V. Shanavas, Z. S. Popović, and S. Satpathy. Theoretical model for rashba spin-orbit interaction in d electrons. *Phys. Rev. B*, 90:165108, 2014. doi:10.1103/PhysRevB.90.165108.

[42] T. Shang, J. Zhao, L.-H. Hu, J. Ma, D. Jakub Gawryluk, X. Zhu, H. Zhang, Z. Zhen, B. Yu, Y. Xu, Q. Zhan, E. Pomjakushina, M. Shi, and T. Shiroka. Unconventional superconductivity in topological kramers nodal-line semimetals. *Science Advances*, 8(43):eabq6589, 2022. doi:10.1126/sciadv.abq6589.

[43] S. Sharma, Sajilesh K. P., A. D. S. Richards, J. Gautreau, M. Pula, J. Beare, K. M. Kojima, S. Yoon, Y. Cai, R. K. Kushwaha, T. Agrawal, E. S. Sørensen, R. P. Singh, and G. M. Luke. Role of spin orbital coupling in unconventional superconductivity, 2022. arXiv:2209.09852.

[44] M. Sigrist and K. Ueda. Phenomenological theory of unconventional superconductivity. *Rev. Mod. Phys.*, 63:239–311, 1991. doi:10.1103/RevModPhys.63.239.

[45] M. Smidman, M. B. Salamon, H. Q. Yuan, and D. F. Agterberg. Superconductivity and spin–orbit coupling in non-centrosymmetric materials: a review. *Reports on Progress in Physics*, 80(3):036501, 2017. doi:10.1088/1361-6633/80/3/036501.

[46] G. V. Subba Rao, K. Wagner, G. Balakrishnan, J. Janaki, W. Paulus, R. Schöllhorn, V. S. Subramanian, and U. Poppe. Structure and superconductivity studies on ternary equiatomic silicides, MM′Si. *Bulletin of Materials Science*, 7:215–228, 1985.

[47] H. J. Vidberg and J. W. Serene. Solving the eliashberg equations by means of n-point padé approximants. *Journal of Low Temperature Physics*, 29(3):179–192, 1977. doi:10.1007/BF00655090.

[48] Z. Wang, P. Zhang, G. Xu, L. K. Zeng, H. Miao, X. Xu, T. Qian, H. Weng, P. Richard, A. V. Fedorov, H. Ding, X. Dai, and Z. Fang. Topological nature of the $FeSe_{0.5}Te_{0.5}$ superconductor. *Phys. Rev. B*, 92:115119, 2015. doi:10.1103/PhysRevB.92.115119.

[49] Q. Wu, S. Zhang, H.-F. Song, M. Troyer, and A. A. Soluyanov. Wanniertools : An open-source software package for novel topological materials. *Computer Physics Communications*, 224:405 – 416, 2018. doi:10.1016/j.cpc.2017.09.033.

[50] T. Y. Yang, Q. Wan, J. P. Song, Z. Du, J. Tang, Z. W. Wang, N. C. Plumb, M. Radovic, G. W. Wang, G. Y. Wang, Z. Sun, Jia-Xin Yin, Z. H. Chen, Y. B. Huang, R. Yu, M. Shi, Y. M. Xiong, and N. Xu. Fermi-level flat band in a kagome magnet. *Quantum Frontiers*, 1(1):14, 2022. doi:10.1007/s44214-022-00017-7.

[51] J.-X. Yin, W. Ma, T. A. Cochran, X. Xu, S. S. Zhang, H.-J. Tien, N. Shumiya, G. Cheng, K. Jiang, B. Lian, Z. Song, G. Chang, I. Belopolski, D. Multer, M. Litskevich, Z.-J. Cheng, X. P. Yang, B. Swidler, H. Zhou, H. Lin, T. Neupert, Z. Wang, N. Yao, T.-R. Chang, S. Jia, and M. Zahid Hasan. Quantum-limit chern topological magnetism in $TbMn_6Sn_6$. *Nature*, 583(7817):533–536, 2020. doi:10.1038/s41586-020-2482-7.

[52] I. Yui, H. Hisatomo, and O. Yoshihiko. YCr_6Ge_6 as a candidate compound for a kagome metal. *Journal of the Physical Society of Japan*, 82(2), 2013. doi:10.7566/JPSJ.82.023705.

[53] N. N. Zhuravlev and A. A. Stepanov. X-ray study of superconduction bismuth–platinum alloy with temperature range of 20–640°. *Kristallografiya*, 7:310–311, 1962.